



저작자표시-비영리-변경금지 2.0 대한민국

이용자는 아래의 조건을 따르는 경우에 한하여 자유롭게

- 이 저작물을 복제, 배포, 전송, 전시, 공연 및 방송할 수 있습니다.

다음과 같은 조건을 따라야 합니다:



저작자표시. 귀하는 원저작자를 표시하여야 합니다.



비영리. 귀하는 이 저작물을 영리 목적으로 이용할 수 없습니다.



변경금지. 귀하는 이 저작물을 개작, 변형 또는 가공할 수 없습니다.

- 귀하는, 이 저작물의 재이용이나 배포의 경우, 이 저작물에 적용된 이용허락조건을 명확하게 나타내어야 합니다.
- 저작권자로부터 별도의 허가를 받으면 이러한 조건들은 적용되지 않습니다.

저작권법에 따른 이용자의 권리는 위의 내용에 의하여 영향을 받지 않습니다.

이것은 [이용허락규약\(Legal Code\)](#)을 이해하기 쉽게 요약한 것입니다.

[Disclaimer](#)

Master of Science

**Effect of two types of polymeric binders
on the performance of high-capacity and
solvent-free electrodes in lithium-ion batteries**

The Graduate School of the University of Ulsan

Department of Chemical Engineering

Min Jae Kim

**Effect of two types of polymeric binders
on the performance of high-capacity and
solvent-free electrodes in lithium-ion batteries**

Supervisor: Professor Eun-Suok Oh

A Dissertation

Submitted to

The Graduate School of the University of Ulsan

In partial Fulfillment of the Requirements

For the Degree of

Master

by

Min Jae Kim

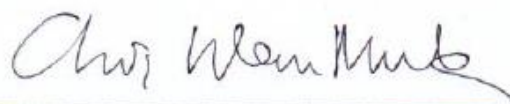
Department of Chemical Engineering

Ulsan, Korea

February 2024

**Effect of two types of polymeric binders
on the performance of high-capacity and
solvent-free electrodes in lithium-ion batteries**

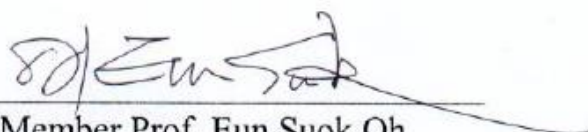
This certifies that the master's thesis
of Min Jae Kim is approved.



Committee Chair Prof. Won Mook Choi



Committee Member Prof. Jeong Hwan Koh



Committee Member Prof. Eun Suok Oh

Department of Chemical Engineering

Ulsan, Korea

February 2024

Acknowledgement

석사 과정을 진행하면서 많은 분들의 도움과 격려를 받아 이 글을 통해 감사의 인사를 전하고자 합니다.

우선, 석사 과정 동안 다양한 프로젝트와 연구 지도를 통해 넓은 식견과 많은 경험을 겪으며 항상 큰 힘이 되어 주신 오은석 교수님께 깊은 감사의 말씀을 드립니다. 이러한 모습을 본받아 저 역시 좋은 연구원이자 훌륭한 어른이 될 수 있도록 노력하겠습니다.

2021년 10월 연구실에 처음 들어왔을 때부터 장비 사용법부터 실험설계법까지 꼼꼼하게 가르쳐 주신 크리스탈 박사님과 남카 연구원님께도 깊은 감사의 말씀을 드립니다. 또한 연구 진행에 도움을 주신 에너지 나노 연구실 선배님, 후배님들과 멋진 경험을 함께해준 100% 팀 팀원들에게도 진심으로 감사의 인사를 전합니다.

항상 저의 결정을 응원해 주시고 지원해 주신 저의 부모님과 저의 인생 멘토 누나 김지혜 님께도 진심으로 감사의 말씀을 드립니다.

마지막으로, 석사 과정 첫 학기부터 항상 제 옆에서 든든한 버팀목이 되어준 제 여자 친구 차승은 씨에게도 진심으로 감사의 말씀을 드립니다.

앞으로도 성실한 자세로 최선을 다하고 매 순간 발전하며 어디서든지 필요로 하는 사람으로 성장해 나가겠습니다.

2024년 2월
김민재 올림

Abstract in Korean

리튬 이차전지는 스마트폰, 무선이어폰, 에너지 저장장치(ESS), 전기자동차와 같은 다양한 분야에 적용되며, 장수명, 고출력을 위한 고에너지 밀도를 갖춘 전지 소재 및 배터리 제조공정에 대한 연구가 활발하게 진행되고 있다. 이처럼 리튬 이온 배터리의 수요가 증가하며 배터리의 원가를 낮추기 위해 전지 소재 성능 향상 및 전지 제조공정 비용 절감 기술이 주목받고 있다.

전지 소재 측면에서 고용량 고출력의 차세대물질로 Si계 음극활물질의 부피팽창을 완화하며 전극에 높은 안정성과 성능 향상에 기여하는 바인더의 중요성이 대두되고 있다. 전지 제조공정 측면에서 고로딩의 전극을 제조할 수 있을 뿐만 아니라 기존의 습식공정 대비 많은 이점을 지니는 건식공정에 대한 연구가 활발히 진행되고 있다. 특히 건식 전극은 용매를 사용하지 않고 전극의 형태를 유지하기 위해 바인더의 역할이 매우 중요하다.

본 연구에서는 SiO_x 5 % ~ 30 % 와 Graphite를 복합 음극활물질로 사용하여 상업용 수분산 바인더 SBR(styrene-butadiene rubber), CMC(carboxy-methyl cellulose)에 적용하였을 때 최적 SiO_x 비율을 연구했다. 이후 SiO_x의 부피팽창에 대한 기계적 안정성을 부여하는 AM monomer와 AA monomer의 자유 라디칼 중합으로 제작된 P(AM-AA) 공중합체 바인더의 성능을 확인하고자 앞선 SiO_x/C 최적 비율의 고용량 음극 전극에 적용했다. 중합한 바인더의 물리화학적 성능을 평가하기 위해 FT-IR, DSC, TGA, Rheology test, 전극저항 평가, 접착력 평가, 전해액 착수 등의 실험과 0.005 ~ 1.5 V 전압 범위에서 사이클 수명, 율속 특성, CV 분석, 임피던스 분석을 진행했다.

또한, 리튬이온 배터리 제조공정에서 기존 습식공정의 한계점을 극복하며 용매를 사용하지 않고 고로딩의 자립형 양극 건식 전극을 제작해 PTFE 고분자 바인더와 PVDF 고분자 바인더의 비율에 따른 건식 전극의 특성 평가 실험을 비교 분석했다. 고로딩의 건식 전극에 적용된 바인더의 물리화학적 성능을 평가하기 위해 전극저항 평가, 접착력 평가 SAICAS 등의 실험과 2.7 ~ 4.2 V 전압 범위에서 사이클 수명, 율속 특성, CV 분석, 임피던스 분석을 진행했다.

Abstract in English

Lithium-ion batteries (LIBs) are being used in various fields such as smartphones, wireless earphones, energy storage system, and electric vehicles. Intensive research efforts are currently being directed towards the development of battery materials and manufacturing techniques, with the goal of producing batteries that boast high energy density, extended longevity, and superior performance. With the rising demand for lithium-ion batteries, there is a growing focus on advancing technologies to enhance the performance of battery materials and to reduce the costs associated with the battery manufacturing process, ultimately aiming to decrease the overall cost of batteries.

Regarding battery materials, the significance of binders is coming to the forefront as a next-generation material. These binders are essential for high-capacity and high-output applications, as they mitigate the volume expansion in silicon-based anode active materials, thereby contributing to the enhanced stability and performance of electrodes. In terms of the battery manufacturing process there is active research on the dry process method. This approach is not only capable of producing high-loading electrodes but also offers numerous advantages compared to the traditional wet process. Specifically, in the case of dry electrodes, the role of the binder becomes crucial in maintaining the electrode's shape, especially as it eliminates the need for a solvent.

In this study, we investigated the optimal SiO_x ratio for application in commercially available water-dispersed binders, namely SBR (styrene-butadiene rubber) and CMC (carboxymethyl cellulose). This was done using a composite anode active material comprised of 5 % to 30 % SiO_x and graphite. Subsequently, to evaluate the performance of the P(AM-AA) copolymer binder, synthesized through free radical polymerization of AM and AA monomers, we applied it to a high-capacity cathode electrode. This was done to assess its mechanical stability against the volume expansion of SiO_x, using the optimal SiO_x/C ratio. To evaluate the physical and chemical performance of the polymerized binder, various experiments were conducted. These included FT-IR, DSC, TGA, rheology tests, evaluations of electrode resistance, adhesion tests, and analyses of electrolyte uptake. Additionally, to assess the cycling performance, rate capability, and CV test within the voltage range of 0.005 to 1.5 V, an EIS test was also performed.

Additionally, moving beyond the usual wet process used in making lithium-ion batteries, we created a high-capacity anode dry electrode without using solvents. We also carried out tests to see how the dry electrode behaves with different amounts of PTFE and PVDF polymer binders. To evaluate the physical performance of the binder applied to the high-loading dry electrode, experiments

such as electrode resistance evaluation, adhesion tests, and SAICAS analyses were conducted. Additionally, to assess the cycling performance, rate capability, and CV test within the voltage range of 2.7 to 4.2 V, an EIS test was also performed.

Table of contents

Acknowledgement -----	I
Abstract in Korean -----	II
Abstract in English -----	IV
Table of contents -----	VI
Figure list -----	X
Table list -----	XII

1. Introduction

1.1. Lithium-ion batteries (LIBs) -----	1
1.2. Manufacturing Process of LIBs -----	3
1.2.1. Conventional wet process -----	3
1.2.2. Challenges and limitations of conventional wet process -----	3
1.3. Solvent-free dry process -----	5
1.4. Necessity of binder research -----	7
1.5. Research Objectives -----	9

2. Experimental methods

2.1. Fabrication of P(AM-co-AA) binder -----	10
2.1.1. Synthesis of poly (acrylamide-co-acrylic acid) -----	10
2.2. Preparation of the slurry film -----	12

2.2.1. SiO _x /C electrode-----	12
2.2.2. SiO _x /C electrodes using P(AM-co-AA) as binder -----	12
2.2.3. Free-standing dry electrode -----	13
2.3. Fabrication of 2032 coin half cells-----	16
2.3.1. SiO _x /C electrode-----	16
2.3.2. SiO _x /C electrodes using P(AM-co-AA) as binder -----	16
2.3.3. Free-standing dry electrode -----	16
2.4. Physical characteristics-----	18
2.4.1. Fourier transform infrared spectroscopy (FT-IR)-----	18
2.4.2. Thermal analysis -----	18
2.4.3. Rheological character -----	18
2.4.4. Field-emission scanning electron microscopy (FE-SEM)-----	18
2.4.5. Electrode resistance-----	19
2.4.6. Electrolyte uptake-----	19
2.4.7. Adhesive strength-----	19
2.4.8. Surface and Interfacial Cutting Analysis System (SAICAS)-----	20
2.5. Electrochemical properties -----	20
2.5.1. Galvanostatic charge and discharge test-----	20
2.5.2. Cyclic voltammetry (CV) and Electrochemical impedance spectroscopy (EIS)-----	20

3. Results and discussion

3.1. SiO _x /C optimal ratio-----	21
3.2. Physical characteristics-----	24

3.2.1. FT-IR results -----	24
3.2.2. Thermal analysis results -----	24
3.2.3. Rheological properties of binder and slurries results-----	28
3.2.4. Electrode resistivity & resistance results-----	31
3.2.5. Electrolyte uptake and adhesive strength results-----	33
3.3. Electrochemical characteristics -----	36
3.3.1. Cycle performance results -----	36
3.3.2. Rate capability results-----	38
3.3.3. Cyclic voltammetry results -----	40
3.3.4. Electrochemical Impedance Spectroscopy results-----	42
3.3.5. Thickness change results after cycling -----	44
3.4 Conclusion -----	46

4. Results and discussion

4.1. Physical characteristics-----	47
4.1.1. Optimal ratio of conductive materials-----	47
4.1.2. Electrode resistivity and resistance results -----	49
4.1.3. Adhesive strength results-----	49
4.1.4. Surface and Interfacial Cutting and Analysis System results -----	52
4.1.5. FE-SEM results -----	52
4.2. Electrochemical characteristics -----	55
4.2.1. Cycle performance and rate capability results -----	55
4.2.2. Cyclic voltammetry results -----	58

4.2.3. Electrochemical Impedance Spectroscopy results-----	58
4.3 Conclusion-----	61
5. Reference-----	62

Figure list

- Figure 1.** Schematic diagram of the charge/discharge process of a LIB.
- Figure 2.** Conventional wet manufacturing process in LIBs.
- Figure 3.** Wet coating process and dry coating process in LIBs.
- Figure 4.** Requirements and desired properties of binders in LIBs.
- Figure 5.** Free radical polymerization between AM and AA monomer.
- Figure 6.** The composition of the (a) wet electrode using CMC/SBR (b) P(AM-AA) as binders and (c) solvent-free dry electrode.
- Figure 7.** Schematic illustration of the manufacturing of (a) wet electrode using CMC/SBR (b) P(AM-AA) as binders and (c) solvent-free dry electrode.
- Figure 8.** CR 2032 coin half cell.
- Figure 9.** (a) Average adhesive strength (b) Composite volume resistivity (c) Initial coulombic efficiency & voltage profile (d) EIS (e) Cycling performance at 0.5C, 100 cycles and (f) Rate capability at vs. C-rate results with each 10 cycles of different ratio of SiO_x/C electrode.
- Figure 10.** FT-IR results of different ratio of AA in P(AM-AA).
- Figure 11.** DSC results of different ratio of AA in P(AM-AA).
- Figure 12.** TGA results of different ratio of AA in P(AM-AA).
- Figure 13.** Rheological properties result of the pure binder (a) viscosity and (b) stress vs. shear rate depending on the ratio of AM and AA monomer.
- Figure 14.** Rheological properties result of the (a) viscosity and (b) stress vs. shear rate depending on the ratio of AM and AA monomer in slurry.
- Figure 15.** (a) Composite volume resistivity and (b) Interface resistance results of different ratio of AA in P(AM-AA).
- Figure 16.** Electrolyte uptake results of different ratio of AA in P(AM-AA).
- Figure 17.** Average adhesive strength results of different ratio of AA in P(AM-AA).
- Figure 18.** Cycling performance at 0.5C of different ratio of AA in P(AM-AA).
- Figure 19.** Rate capability at vs. C-rate with each 10 cycles of different ratio of AA in P(AM-AA).
- Figure 20.** CV curve results of different ratio of AA in P(AM-AA).
- Figure 21.** EIS results expressed as different ratio of AA in P(AM-AA).
- Figure 22.** Thickness change results after 100 cycles expressed as different ratio of AA in P(AM-AA).
- Figure 23.** (a) MWCNT (b) Super P and (c) physical mixing of both MWCNT and Super P at C-rate with each 5 cycles and voltage range from 2.7 V to 4.2 V in solvent-free dry electrode.

Figure 24. (a) Interface resistance and (b) composite volume resistivity results of different ratio of PTFE and PVDF binder in solvent-free dry electrode.

Figure 25. Average adhesive strength results of different ratio of PTFE and PVDF binder in solvent-free dry electrode.

Figure 26. (a) 100:0 (b) 75:25 (c) 50:50 (d) average horizontal force and (e) SAICAS images of different ratio of PTFE and PVDF binder in solvent-free dry electrode.

Figure 27. FE-SEM images PTFE fibrilization of solvent-free dry electrode with different magnification: (a) 20,000x, (b) 25,000x, (c) 100,000x and (d) 100,000x.

Figure 28. Cycling performance at 1C of different of PTFE and PVDF binder in solvent-free dry electrode.

Figure 29. Rate capability at vs. C-rate with each 5 cycles of different of PTFE and PVDF binder in solvent-free dry electrode.

Figure 30. (a) 100:0 (b) 75:25 and (c) 50:50 CV curves of different ratio of PTFE and PVDF binder in solvent-free dry electrode.

Figure 31. EIS results expressed as different ratio of PTFE and PVDF binder in solvent-free dry electrode.

Table list

Table 1. EIS results expressed as different ratio of SiO_x/C electrode.

Table 2. EIS results expressed as different ratio of AA in P(AM-AA).

1. Introduction

1.1. Lithium-ion batteries (LIBs)

Since Sony Corporation's initial commercialization of lithium-ion batteries (LIBs) in 1991, LIBs have expanded their application everywhere, from smartphones and Bluetooth headsets to electric vehicles. As a result, LIBs have become one of the most vital energy devices, deeply influencing and changing human life [1-3].

LIBs consist of anode and cathode electrodes, which are immersed in an electrolyte solution and are isolated from each other by a separator. Both electrodes are composed of active materials, a conductive agent, a binder, and a current collector. The energy of the electrode in LIBs is primarily determined by the active materials, while the addition of a conductive agent enhances the electrode's rate capability by facilitating more efficient electron transport. Furthermore, a binder is employed to cohesively adhere the active materials and the conductive agent to the current collector [4-6]. In LIBs, the potential difference between the two electrodes produces electron movement through the external circuit and ion movement within the electrolyte, resulting in energy generation through redox reactions. In the case of secondary batteries, the anode where the oxidation reaction occurs and the cathode where the reduction reaction occurs are distinguished based on the spontaneous discharge process. In the discharge process of a LIB, electrons move from the anode to the cathode through an external circuit, and lithium ions move to the cathode through the electrolyte, converting chemical energy into electrical energy. Inversely, in the charge process, electrons move from the cathode to the anode through an external conductor by a voltage applied above the equilibrium potential difference, and the lithium ions of the cathode active material move to the anode through the electrolyte, converting electrical energy into chemical energy and storing energy [7-11]. In this manner to increase the efficiency of lithium-ion batteries (LIBs), extensive research has been conducted on a variety of electrode materials and battery manufacturing process techniques [12].

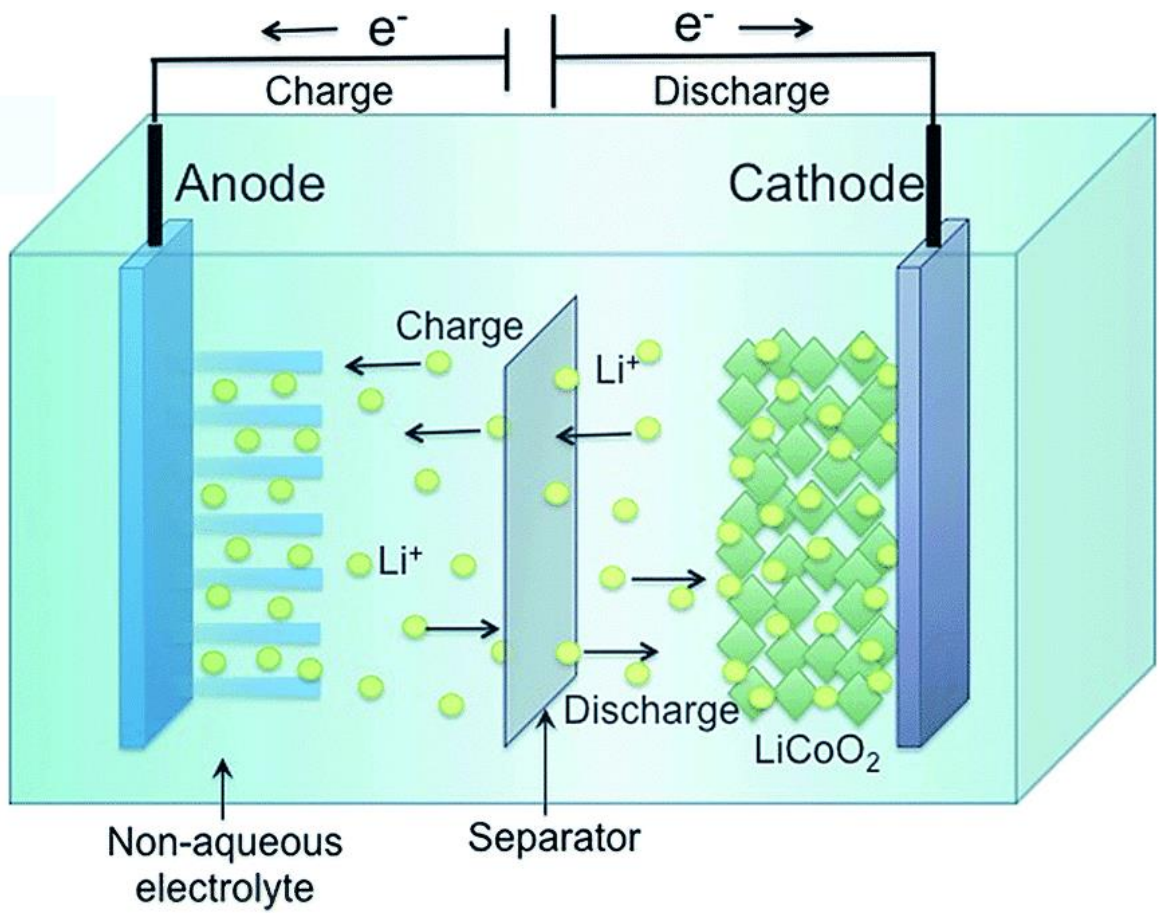


Figure 1. Schematic diagram of the charge/discharge process of a LIB

1.2. Manufacturing Process of LIBs

1.2.1. Conventional wet process

Figure 2. illustrates the standard commercial electrode manufacturing process. In this procedure, the active material, conductive material, and polymer binder are uniformly mixed with a solvent to create a slurry of suitable viscosity using a mixer. Typically, deionized water is utilized as a solvent for the anode, while N-methyl pyrrolidone (NMP), an organic solvent, is used at the cathode [13,14]. This prepared slurry is then applied onto substrates through a slot-die coating machine, with the anode being placed on copper foil and the cathode on aluminum foil [15]. The coated substrates are dried in a large oven. The drying process, executed at high temperatures, aims to rapidly evaporate the solvent. While the drying temperature depends on the specific material, solvent, and coating speed, it is generally set around 100 °C in commercial electrode manufacturing. After drying, the electrodes are compressed under high pressure in a calendaring machine to achieve the desired thickness and a dense structure [16,17].

1.2.2. Challenges and limitations of conventional wet process

The drying process in electrode manufacturing is a significant energy consumer, accounting for over 47% of the total process energy usage. The associated equipment, often extending up to 50 meters, occupies a substantial factory space [18]. Additionally, the cathode manufacturing process presents environmental challenges due to the necessity of recovering N-methyl pyrrolidone (NMP), an organic solvent. Current research is also focused on increasing the energy density of lithium-ion batteries (LIBs) by enhancing the active material thickness within the same volume. However, the existing wet process has limitations, particularly in exceeding an active material thickness of 100 μm . During drying process, the binder tends to migrate to the surface due to capillary forces, leading to uneven distribution. This results in reduced cohesion among electrode particles and weak adhesion between the current collector and the composite layer, thereby diminishing electrode performance [19-21]. To manufacture next-generation electrodes, such as those in all-solid-state batteries, precise control over the thickness of high-loading electrodes is crucial. In response to these challenges, there is an increasing focus on research into solvent-free dry electrode [23]. This approach is aimed at overcoming the limitations associated with wet processes, which notably include high energy consumption, environmental hazards, significant investment in equipment, and diminished production efficiency [22,24,25].

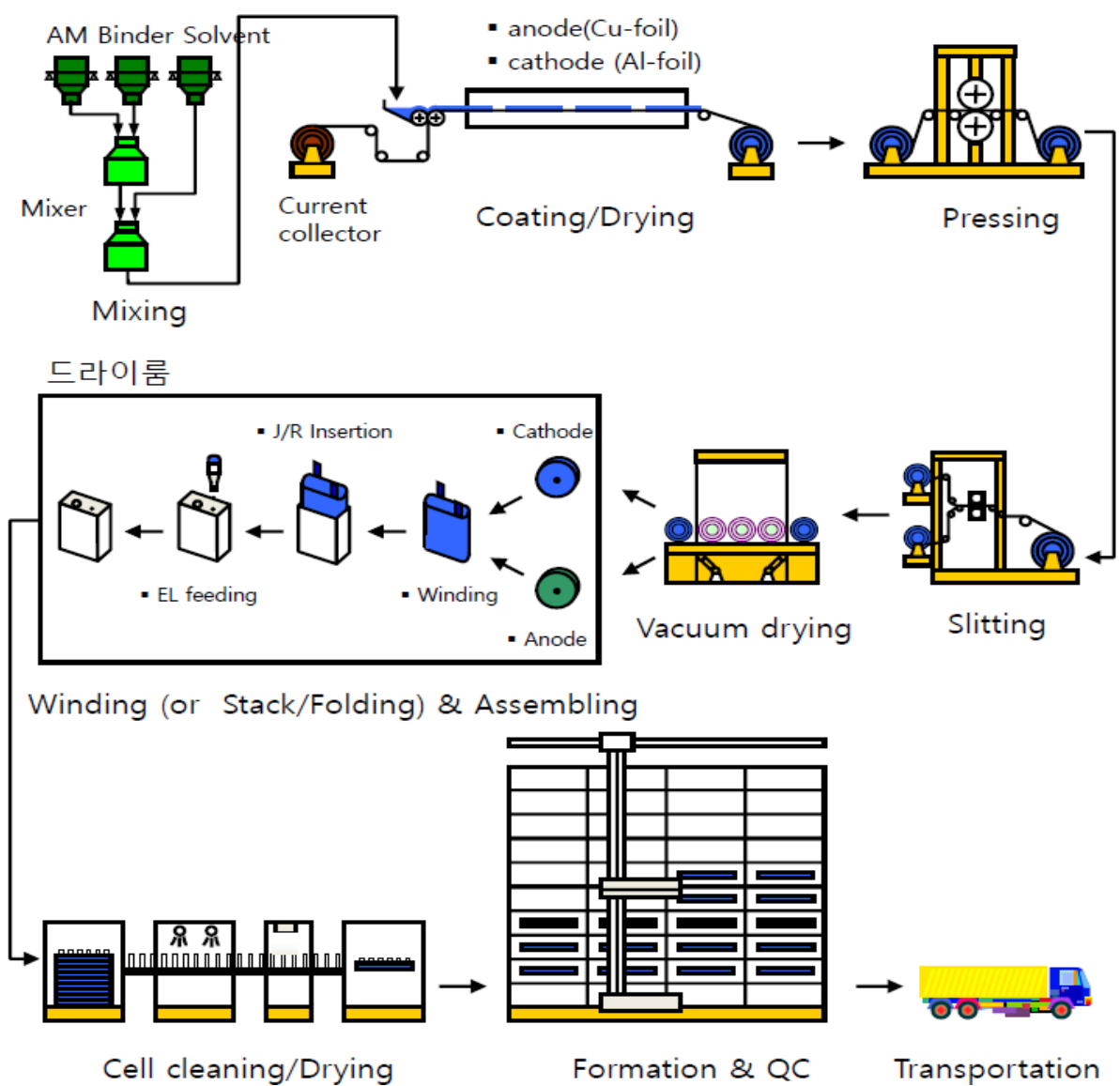


Figure 2. Conventional wet manufacturing process in LIBs

1.3 Solvent-free dry process

There are various solvent-free electrode fabrication methods, including dry spraying deposition, vapor deposition, 3D printing, direct pressing, hot melting and extrusion, and polymer fibrillation. Generally, most of the solvent-free electrode fabrication procedures have three steps, i.e., dry mixing, dry coating, and final pressing to achieve the desired thickness and dense electrode structure [26]. Herein, there are some advantages of solvent-free dry electrode. First, using a solvent-free dry process could cut costs in three ways: it uses less energy, needs fewer raw materials, and requires a smaller investment. Therefore, the overall cost could go down by 10 % to 15 %. Second, in contrast to conventional wet processes, the omission of electrode coating and drying in the electrode fabrication process substantially decreases CO_2 . Also, there's no need to recover organic solvents like N-Methyl-2-pyrrolidone (NMP), making the process more eco-friendly and cost-effective. Third, improved electrode quality can be fabricated. In the wet process, when the solvent evaporates during drying, it makes the electrode more porous. However, the dry process results in less porosity compared to the wet process, which contributes to higher energy density and better performance. Also, in the drying of the wet process, the fast solvent evaporation results in a binder distribution gradient along the radial direction of the electrodes. On the other hand, in the dry process, the uniform distribution of the binder increases the contact between the current collector and the electrode film, as well as between the active materials, thereby enhancing mechanical strength. This attribute significantly benefits the fabrication of electrodes with high loading and thick films. Owing to these benefits, it is imperative to conduct research and development on the solvent-free dry process, in order to propel the advancement of high-capacity, high-performance next-generation lithium-ion batteries [27-30].

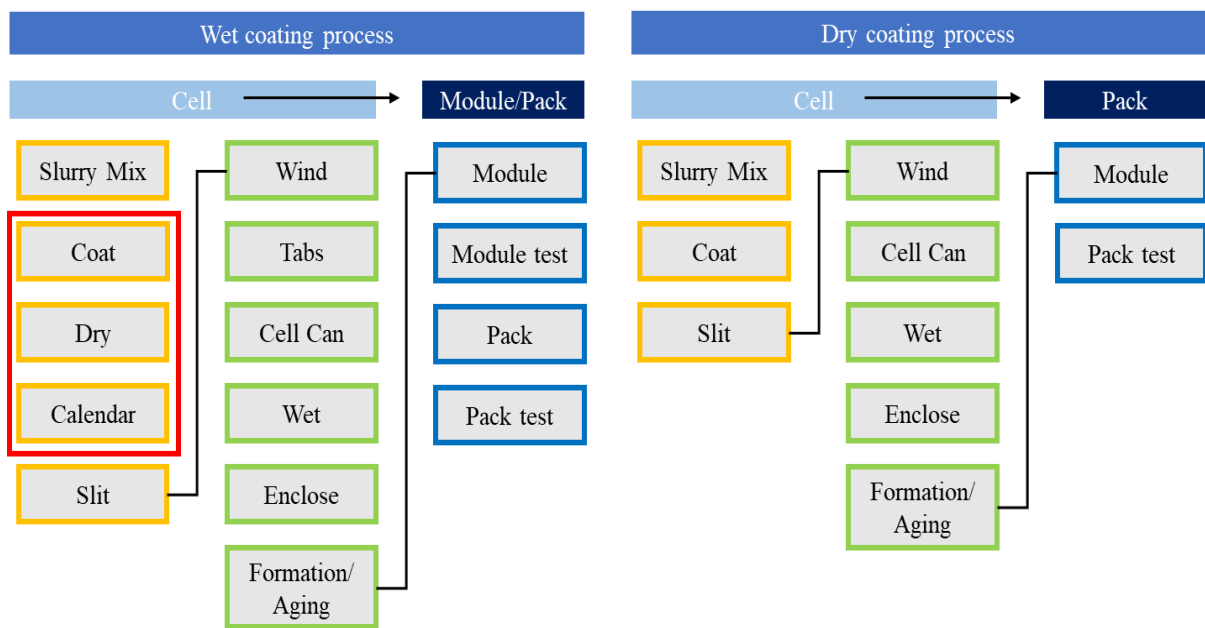


Figure 3. Wet coating process and dry coating process in LIBs

1.4. Necessity of binder research

Recently, silicon has emerged as a promising candidate for anode active materials in next-generation high-energy lithium-ion batteries. In this context, the role of binders is becoming increasingly critical, particularly in mitigating the challenge of volume expansion, which is a major issue with silicon anodes [31-33]. Binders play an important role in the electrode manufacturing process by ensuring the uniform distribution and effective dispersion of other components within the solvent [34,35]. Binders are essential in promoting ion transport across the electrode-electrolyte interface and play a key role in preventing electrolyte depletion and corrosion of the electrode [36,37]. Moreover, binders are crucial in maintaining the cohesion between the active and conductive materials within the electrode, as well as the adhesion between the current collector and the composite layer throughout the cycling process [38,39]. Figure 4 shows that binders must possess not only chemical and electrochemical safety characteristics but also thermal and mechanical properties [40]. Water-soluble binders fulfill these criteria effectively. Additionally, it is imperative for the binder to maintain stability at both high and low voltages at the anode and cathode during operation, ensuring that it does not react with other materials in the system. Currently commercially available binders cannot maintain the structural stability of silicon electrodes during charge and discharge processes. The prevalent Carboxymethyl cellulose (CMC)/styrene-butadiene rubber (SBR) binder demonstrates inferior mechanical properties, primarily due to inadequate bonding strength between silicon particles and SBR [41-44].

Additionally, In the solvent-free dry process, the role of the binder is crucial in maintaining the form of the electrode without the use of solvents. Among these, research is actively being conducted on the roll-to-roll manufacturing process, which is easily adaptable to conventional electrode processes. This approach primarily utilizes polymer fibrillization techniques, which were initially developed by Maxwell Technologies for producing activated carbon electrodes in supercapacitors [45-47]. The method includes the use of fibrillizable polytetrafluoroethylene (PTFE), capable of undergoing fibrillation under high shear force to create PTFE fibrils. The fibrils produced have the capacity to bind particles of active material without surrounding them, and they can be subjected to hot pressing to fabricate self-supporting electrode films. These PTFE polymer binders enhance the mechanical strength of the electrode film in the solvent-free dry electrode [48-52].

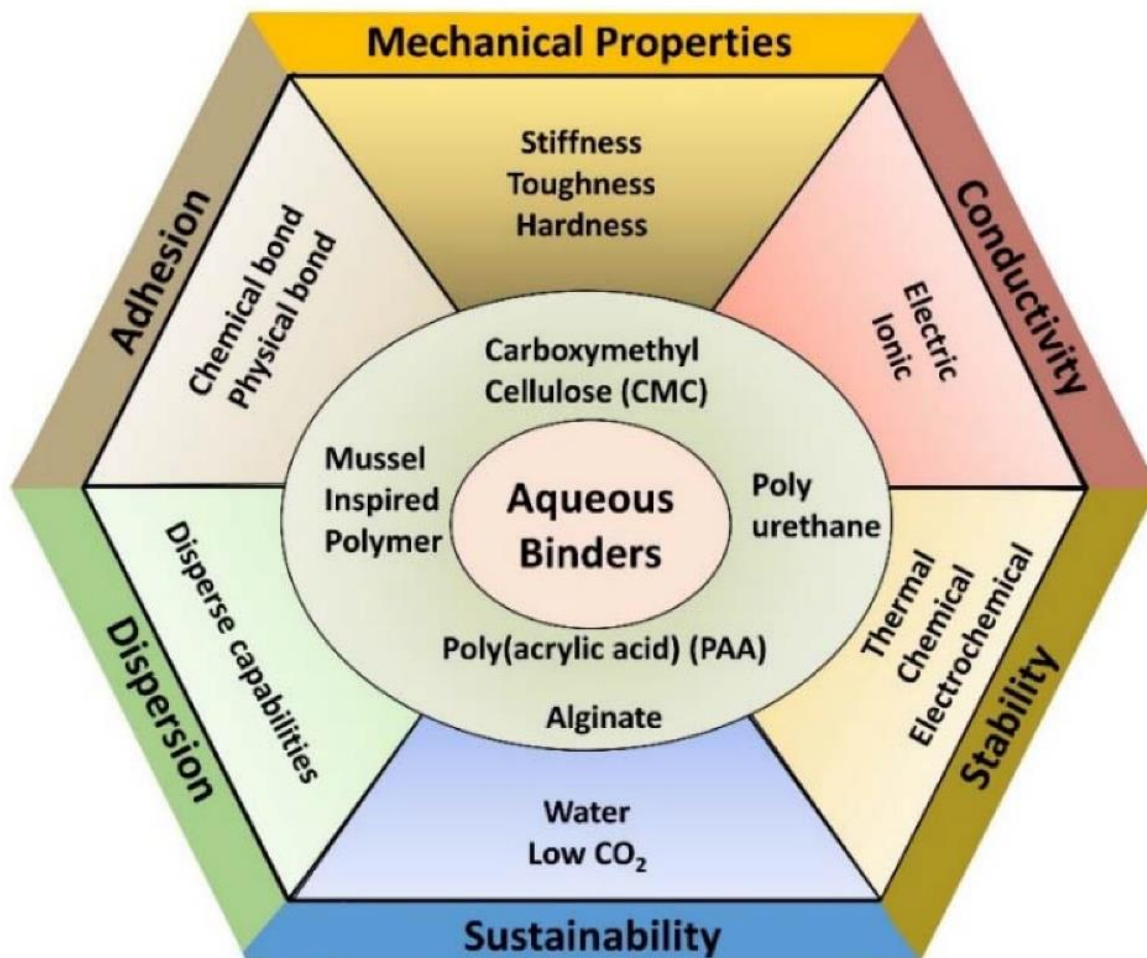


Figure 4. Requirements and desired properties of binders in LIBs

1.5. Research Objectives

In this study, we investigate the optimal mixing ratio for SiO_x/C composite materials. Based on this, the carboxylic group (-COOH) in acrylic acid (AA) and the hydroxyl group (-OH) on the SiO_x surface undergo a heating process at approximately 54 °C. This facilitates the formation of a covalent bond through a dehydration condensation reaction, where water is eliminated. Additionally, the amide group (-NH) in acrylamide (AM) and the hydroxyl group (-OH) on the SiO_x surface form a non-covalent hydrogen bond. This experimental approach is driven by the hypothesis that the synergistic effect of these covalent and non-covalent bonds can significantly enhance the mechanical stability and electrochemical performance of SiO_x/C anode electrode.

Recent research efforts are increasingly focused on solvent-free dry electrode processes to overcome the limitations of wet processes, including high energy consumption, environmental hazards, significant equipment investment costs, and low production efficiency [53,54].

In this study, high-loading, solvent-free dry electrodes were fabricated using a PTFE polymer binder that undergoes fibrillization under shear force at 19 °C, without the use of solvents. Additionally, prior to the binder comparison evaluation, the optimal ratio of active material to conductive agent was identified through the compounding of the conductive material. Utilizing these ratios, a comparative evaluation was conducted between the PTFE polymer binder and the traditional PVDF polymer binder used in wet processes, based on their respective proportions.

2. Experimental methods

2.1. Fabrication of P(AM-co-AA) binder

2.1.1. Synthesis of poly (acrylamide-co-acrylic acid)

The poly (acrylamide-co-acrylic acid) P(AM-co-AA) was synthesized by free radical polymerization between acrylamide and acrylic acid monomers in an aqueous system, as shown in Figure 5. While adjusting the mass ratio of acrylamide and acrylic acid monomers, maintain a constant initiator system. Both 7.5 g of acrylamide monomer (AM, Sigma Aldrich Co. Ltd) and 7.5 g of acrylic acid (AA, Junsei chemical. Co. Ltd) were dissolved in 70 ml of distilled water over 30 minutes in a 250 ml three-necked flask at about 250 rpm. The flask was equipped with, a thermometer, a reflux condenser, a mechanical stirrer, and a nitrogen line. The solution was then heated to 54 °C in a water bath, and the temperature was maintained throughout the subsequent polymerization process. Prior to the addition of a free radical initiator, the pH was adjusted to 8 using 1 wt.% NaOH. Additionally, nitrogen bubbling was conducted for 40 minutes to remove oxygen from the solution, as oxygen readily inhibits free radical polymerization. For the polymerization of AM, 0.09 g of potassium persulfate (KPS, Sigma Aldrich Co. Ltd) initiator was first added to the solution. After 40 minutes, 0.083 g of tetramethyl-ethylenediamine (TEMED, Sigma Aldrich Co. Ltd) was added as a reaction accelerator. The weight ratios of KPS and TEMED to the total monomer content are 0.006 and 0.0055, respectively. This free radical polymerization was continued for 5 h to completely produce P(AM-co-AA). The resulting viscous solution was precipitated using acetone and then washed twice with a mixture of ethanol and water to remove unreacted monomers and small molecules. After that, the precipitate was dried in a vacuum oven overnight, followed by stirring for 12 hours at room temperature. Other copolymers P(AM-co-AA) with 7:3 and 3:7 weight ratios of AM to AA were synthesized using the same polymerization method, with the total weight of the monomers kept constant at 15 g.

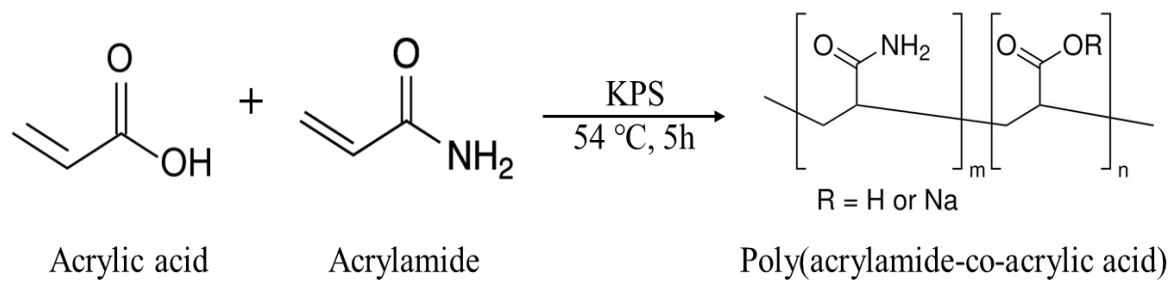


Figure 5. Free radical polymerization between AM and AA monomer.

2.2. Preparation of the slurry film

2.2.1. SiOx/C electrode

Each electrode was fabricated using different ratios of SiOx and Graphite. Binder used as CMC (1.2 wt.%) and SBR (2.3 wt.%). The slurry for the SiOx and graphite electrodes was composed of 96.45 wt.% active materials and 0.05 wt.% conductive materials. Herein, 0.4 % by weight of single-walled carbon nanotubes (SWCNT, OCSiAl) as conductive materials was dissolved in 0.6 % carboxymethyl cellulose (CMC) to control dispersion, along with 3.5 wt.% of a binder and used distilled water solvent to adjust the viscosity of the slurry. The slurry was mixed by Thinky mixer (ARE-310, MDBROS). First, dry mixing with SiOx and graphite were mixed under conditions of 1500 rpm, 1 minutes. Then half of distilled water and SWCNT were added mixed under conditions of 2000 rpm, 3 minutes rotation and 2 times. Then, the binder and the remaining distilled water were added and finally mixed under the same conditions. The mixed slurry was coated with a coater (MC-30, Hohsen) at a coating speed of 9 mm/s onto an 18 μm thick Cu foil. It was then dried for 30 minutes in a convection oven set at 60 °C. Before electrodes were used to make coin half cells, the electrodes were punched of diameter 14, then pressed by roll press machine, and eventually dried for one day at a vacuum oven of 70 °C. The mass loading of electrodes was controlled to be around $8.0 \pm 0.3 \text{ mg/cm}^2$.

2.2.2. SiOx/C electrodes using P(AM-co-AA) as binder

Using the optimal active material ratio of SiOx/C, which was the result of previous experiments, electrodes were fabricated according to the binder ratio.

The slurry for the SiOx and graphite electrodes was composed of 96.45 wt.% active materials and 0.05 wt.% conductive materials. Specifically, 0.4 % by weight of SWCNT was dissolved in 0.6% CMC to control dispersion, along with 3.5 wt.% of a binder and used distilled water solvent to adjust the viscosity of the slurry. The slurry was mixed by Thinky mixer. First, dry mixing with SiOx and graphite were mixed under conditions of 1500 rpm, 1 minutes. Then half of distilled water and SWCNT were added mixed under conditions of 2000 rpm, 3 minutes rotation and 2 times. Then, the binder and the remaining distilled water were added and finally mixed under the same conditions. The mixed slurry was coated with a coater at a coating speed of 9 mm/s onto an 18 μm thick Cu foil. It was then dried for 30 minutes in a convection oven set at 60 °C. Before electrodes were used to make coin half cells, the electrodes were punched of diameter 14, then pressed by roll press machine, and eventually dried for one day at a vacuum oven of 70 °C. The mass loading of electrodes was controlled to be around $5.0 \pm 0.3 \text{ mg/cm}^2$.

2.2.3. Free-standing dry electrode

The slurry of the NCM622 was composed of 70 wt.% active materials and 20 wt.% conductive materials. Specifically, 15 % by weight of Super P and 5 % MWCNT to control dispersion and loading level, along with 10 wt.% of binder. The dry slurry was mixed by powder mixer (WC-MLS300, Wellcos Co.) under conditions of 15000 rpm, 3 minutes rotation and 3 times. Employing a kneader (WC-K100KP, Wellcos Co.), a strong shear force is exerted at 109 °C, resulting in the fiberization of the PTFE binder to form a dough-like consistency. This dough grinds uniformly by using powder mixer. Free-standing electrodes are fabricated using 3-roll mill (WC-3R80B, Wellcos Co.) at a temperature of 100 °C. After adjusting the target electrode thickness through roll pressing, dry electrodes are produced by laminating them onto carbon-coated (Al) foil at a temperature of 80 °C. Before electrodes were used to make coin half cells, the electrodes were punched of diameter 14, and eventually dried for one day at a vacuum oven of 120 °C. The mass loading of dry electrodes was controlled to be around 19.0 mg/cm².

Components		Total (%)	Loading (mg/cm²)	
(a)	Active Materials	SiOx	8	
		Graphite		96.45
	Conductive Material	SWCNT		0.05
	Binder	CMC 1% solution		1.2
		SBR 40%		2.3
Total		100		

Components		Total (%)	Loading (mg/cm²)	
(b)	Active Materials	SiOx	5	
		Graphite		96.45
	Conductive Material	SWCNT		0.05
	Binder	P(AM-AA)		3.5
	Total			100

Components		Total (%)	Loading (mg/cm²)	
(c)	Active Materials	NCM 622	19	
		Super P		70
	Conductive Material	MWCNT		5
				15
	Binder	PTFE		10
		PVDF		10
Total		100		

Figure 6. The composition of the (a) wet electrode using CMC/SBR (b) P(AM-AA) as binders and (c) solvent-free dry electrode

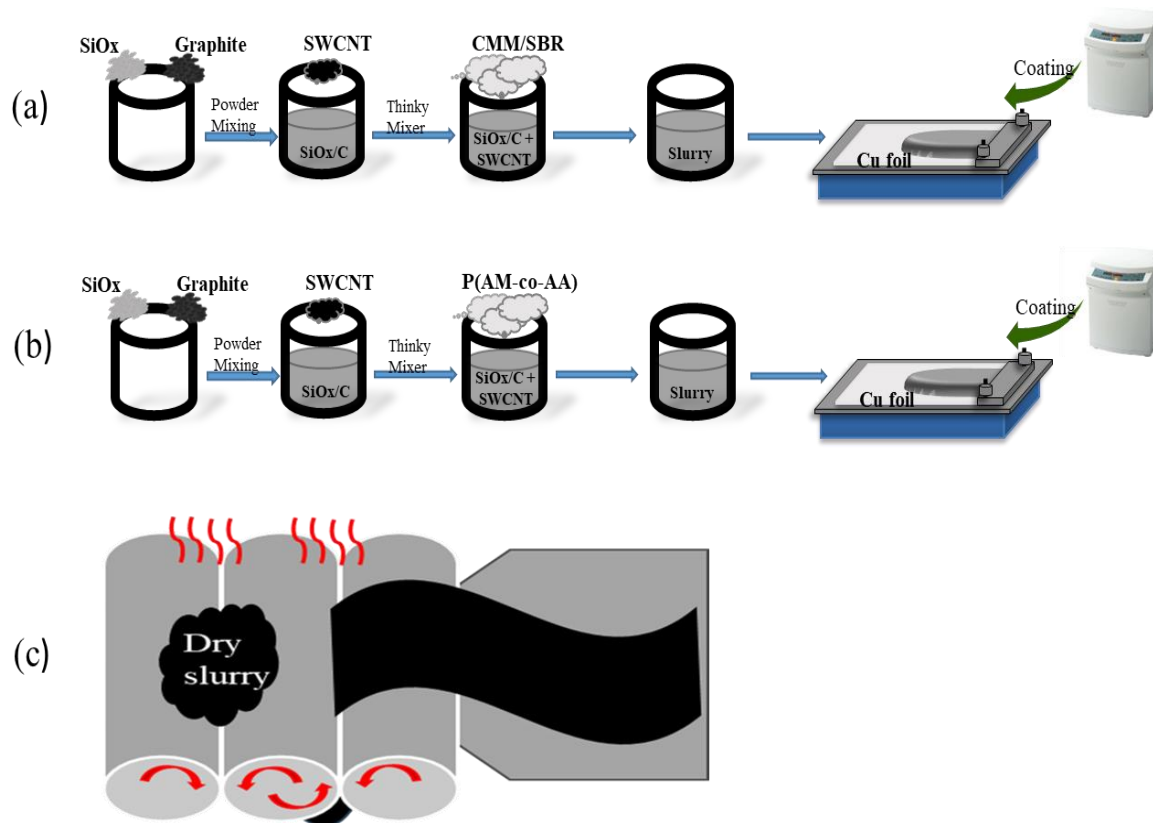


Figure 7. Schematic illustration of the manufacturing of (a) wet electrode using CMC/SBR (b) P(AM-AA) as binders and (c) solvent-free dry electrode

2.3. Fabrication of 2032 coin half cells

2.3.1. SiO_x/C electrode

For electrochemical characterization, 2032 coin-half cells (CR 2032) were assembled in an argon-filled glove box. The assembly used SiO_x/C as the working electrode, Li chips as the counter and reference electrode, and a polypropylene film (W-Scope) as the separator. The electrolyte was a mixture of lithium hexafluorophosphate (1.15M LiPF₆) dissolved in a mixture of solvent ethylene carbonate (EC), fluoroethylene carbonate (FEC), propylene carbonate (PC), diethyl carbonate (DEC), and ethyl methyl carbonate (EMC) in a volume ratio of 20:10:5:40:25. Each coin-half cell was allowed to rest for one day before undergoing electrochemical tests.

2.3.2. SiO_x/C electrodes using P(AM-co-AA) as binder

It is the same as the coin cell manufacturing method above. The assembly used SiO_x/C as the working electrode, Li chips as the counter and reference electrode. The electrolyte was a mixture of lithium hexafluorophosphate (1.15M LiPF₆) dissolved in a mixture of solvent ethylene carbonate (EC), diethyl carbonate (DEC), and ethyl methyl carbonate (EMC) in a volume ratio of 30:40:30 with additive 2 wt.% FEC and 2 wt.% VC.

2.3.3. Free-standing dry electrode

It is the same as the coin cell manufacturing method above. The assembly used solvent-free dry electrodes as the working electrode, Li chips as the counter and reference electrode. The electrolyte was a mixture of lithium hexafluorophosphate (1.15M LiPF₆) dissolved in a mixture of solvent ethylene carbonate (EC), fluoroethylene carbonate (FEC), propylene carbonate (PC), diethyl carbonate (DEC), and ethyl methyl carbonate (EMC) in a volume ratio of 20:10:5:40:25. Each coin-half cell was allowed to rest for one day before undergoing electrochemical tests.

➤ **Coin Half Cell (2032)**

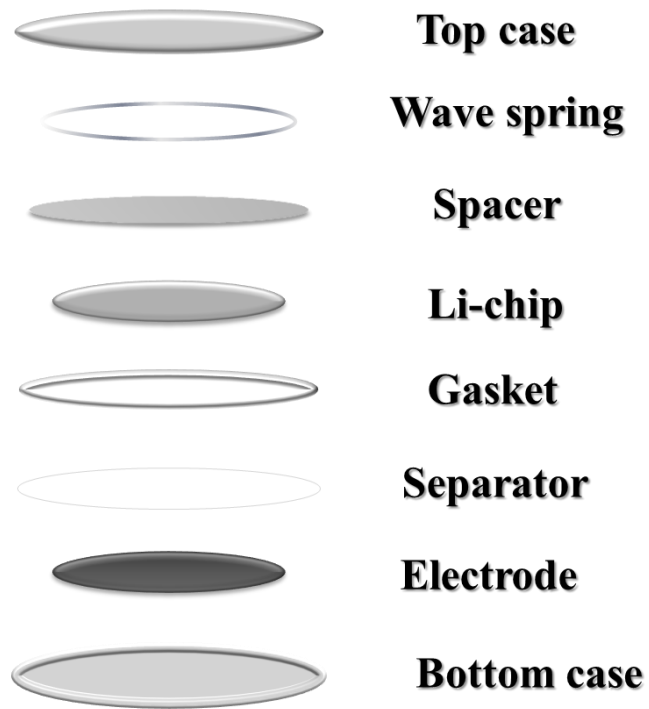


Figure 8. CR 2032 coin half cell

2.4. Physical characteristics

2.4.1. Fourier transform infrared spectroscopy (FT-IR)

Infrared spectrum refers to an analysis method that measures the absorption of energy corresponding to the vibration and rotation of the molecular skeleton whose dipole moment changes by shining infrared rays on the sample. This is because different substances have unique atomic combinations, and no two compounds can produce completely identical substances. Therefore, the infrared spectrum can be used to reliably identify any substance. FT-IR (Nicolet IR 200, Thermo Scientific) spectra from 4000 to 500 cm^{-1} using potassium bromide pellets.

2.4.2. Thermal analysis

For the DSC (Q20, TA Instruments) was performed to identify the glass temperature (T_g) of binders in nitrogen atmosphere. The samples in aluminum cell are scanned from 40 to 240 $^{\circ}\text{C}$ at the heating rate of 10 $^{\circ}\text{C min}^{-1}$ compared with air reference samples.

Thermal analysis of P(AM-co-AA) copolymers were carried out with thermal analyzer in nitrogen atmosphere using the Q50 in TA Instruments. The thermogravimetric analyze (TGA) was performed from initially room temperature to 700 $^{\circ}\text{C}$ with a heating rate of 10 $^{\circ}\text{C min}^{-1}$. The sample was placed in platinum pan.

2.4.3. Rheological character

All rheological properties were measured using a parallel plate rheometer (HR-20, TA Instruments). The samples were heated to a consistent temperature of 25 $^{\circ}\text{C}$ using a Peltier plate. To ensure thermal equilibrium, each sample was given a waiting time and pre-shear period of 180 seconds after being placed on the plate. Following each measurement, a relaxation interval of 30 seconds was implemented to alleviate any deformation from the previous step. For measurements involving the P(AM-co-AA) pure binder and slurries, a 40 mm diameter parallel plate was utilized.

2.4.4. Field-emission scanning electron microscopy (FE-SEM)

The surface morphology of both the SiO_x/C electrode and the dry electrode was examined using field emission scanning electron microscopy (FE-SEM, JEOL JSM-6500F). After the cycling test, cracks were observed on the surface of the electrode. Additionally, the dry electrodes exhibited visible elongation of the PTFE binder.

2.4.5. Electrode resistance

The electrical resistance of the electrodes was measured using a 46 multipoint probe system (RM2610, HIOKI E.E. Co.). The electrode preparation involved slitting to a width of 40 mm, followed by either pressing with a roll press or leaving it unpressed. Subsequently, measurements of the composite layer's volume, surface, and interfacial electrode resistance were systematically taken at regular intervals from the bottom to the top of the electrode.

2.4.6. Electrolyte uptake

The electrolyte uptake of the binder films was also studied through an electrolyte absorption test. These films were prepared using a cast solution method in a Teflon evaporation dish, dried at 60 °C overnight, and then each sample was weighed. Dried binder film was initially weighted (W_{before}), then immersed for 24h at room temperature in mixed solvent consisting of solvent ethylene carbonate (EC), fluoroethylene carbonate (FEC), propylene carbonate (PC), diethyl carbonate (DEC), and ethyl methyl carbonate (EMC) in a volume ratio of 20:10:5:40:25. Afterward, it was weighted (W_{after}) again following the removal of excess electrolyte from its surface. The swelling ratio was calculated as:

$$s = \frac{W_{after} - W_{before}}{W_{before}} \times 100\%$$

2.4.7. Adhesive strength

The mechanical adhesive strength of the coated slurry on the current collector was evaluated using a 180° peel test, conducted with a texture analyzer (TA-PLUS, Lloyd Instrument Ltd.). Adhesion is a critical property for enduring the deformations associated with volume expansion during charging and discharging cycles. The sample preparation process was as follows: Electrodes were initially cut to a width of 2 cm. Subsequently, one side of double-sided tape was adhered to a metal plate, with the opposite side attached to the electrodes. Uniform pressure was ensured by passing the electrodes through a rolling machine twice. The adhesive strength was measured by the texture analyzer, which pulled the electrodes from the metal plate and recorded the adhesion force.

2.4.8. Surface and Interfacial Cutting Analysis System (SAICAS)

The adhesion strength at the interface between the cathode composite and the current collector was measured using the SAICAS. For these measurements, a boron nitride blade with a width of 1 mm was employed, featuring a shear angle of 45°, a rake angle of 20°, and a clearance angle of 10°. During testing, the blade advanced horizontally at a rate of 5 µm/s. In the cutting mode, the blade also descended vertically at 0.5 µm/s until it contacted the carbon-coated aluminum current collector. The adhesion strength was determined by averaging the horizontal forces recorded during the peel mode and then dividing this average by the width of the blade. To ensure accuracy and reliability, at least three measurements were conducted for each sample.

2.5 Electrochemical properties

2.5.1. Galvanostatic charge and discharge test

The electrochemical properties were conducted by the cycling performances in the voltage window of 0.005 to 1.5 V at 0.1C for the first 2 cycles, and 0.5C for the next 100 cycles in anode electrode. On the other hand, the voltage window of 2.7 to 4.2V at 0.2C for the first 3 cycles, and 1C for the next 200 cycles in cathode electrode. The rate capacity test was carried out at various current rate range of 0.1C to 10C with final returning back to 0.1C current rate and each current rate is scanned 10 times at related constant current rate in anode coin-half cell. Dry electrode cathode coin-half cell was carried out at various current rate range of 0.2C to 10C with final returning back to 0.2C current rate and each current rate is scanned 5 times at related constant current rate. All above tests were conducted by TOSCAT-3100 system (TOYO system. Co., LTD Japan) and PEB0501 system (PNE solution. Co., Korea).

2.5.2. Cyclic voltammetry (CV) and Electrochemical impedance spectroscopy (EIS)

Cyclic voltammograms (CV, VSP, BioLogic Science Instruments) of was measured at 0.2 mV/s from 0.005 to 1.5 V in anode coin-half cell and 0.2 mV/s from 2.7 to 4.2 V in dry electrode cathode coin-half cell.

Electrochemical impedance spectroscopy (EIS) was tested into potentiostatic mode that is fixed with AC amplitude of 5 mV in anode coin-half cell and 10mV in dry electrode cathode coin-half cell at a frequency range 10^{-3} to 10^6 Hz. The open circuit voltage (OCV) in EIS measurements was controlled 0.2 V vs. Li/Li^+ . Nyquist plot was fitted by the equivalent circuit.

3. Results and discussion

3.1. SiO_x/C optimal ratio

We fabricated a anode electrode exhibiting high capacity, incorporating a composite of 5-30 wt.% SiO_x in the SiO_x/graphite as the anode active material, and subsequently performed an evaluation to determine the optimal composition ratio.

The increase in composite resistivity (before press samples) due to the higher amount of SiO_x, which has lower conductivity compared to graphite, is illustrated in Figure 9 (b). The increase in the initial voltage drops of discharge curves, as shown in Figure 9 (c), is attributed to the rising amount of SiO_x. As generally known, the increase in the amount of SiO_x increases irreversibility in capacity. EIS impedance in Figure 9 (d) implies that the electrochemical kinetics of SiO_x become easier than the electrochemical kinetics of graphite because the R_{ct} becomes smaller as the SiO_x increases, even though the electrical conductivity of the SiO_x is smaller than graphite. More surprisingly, the cyclic performance in Figure 9 (e) indicates that no apparent capacity fading observed at most of high-capacity anodes occurs up to 30 wt.% SiO_x. The rate capability depicted in Figure 9 (f) demonstrates that it is sufficient for application in commercial cells. In particular, the discharge capacity is fully recovered from the high current rate 2C to 0.1C, indicating no significant damage in the SiO_x/C electrode. This must be contributed to the electrolyte containing large amount of fluoroethylene carbonate (FEC) additive, 10 %. Electrolyte additives are one of the most effective ways for improving the performance of high-capacity Li-ion batteries. The effect of the additive/cosolvent FEC was found to drastically improve the capacity retention and coulombic efficiency of the cells despite its disadvantage such as the formation of HF.

In conclusion, the SiO_x-25 % and Graphite composite, used as an anode active material and characterized by its highest adhesive properties and excellent electrochemical stability, was found to have the best performance.

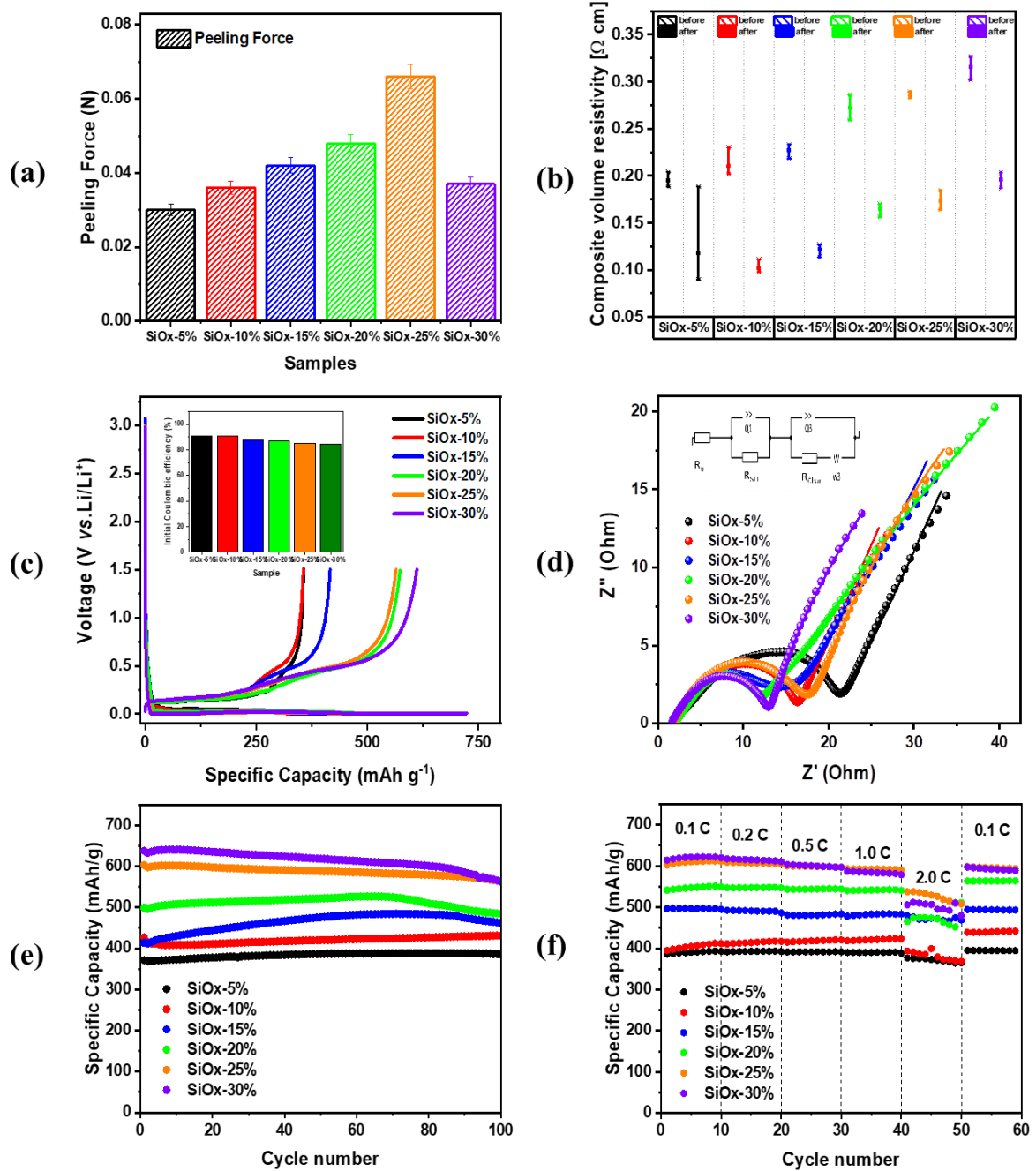


Figure 9. (a) Average adhesive strength (b) Composite volume resistivity (c) Initial coulombic efficiency & voltage profile (d) EIS (e) Cycling performance at 0.5C, 100 cycles and (f) Rate capability at vs. C-rate results with each 10 cycles of different ratio of SiOx/C electrode

SiO _x /C electrode	Resistance, R (Ω)			
	<i>R_b</i>	<i>R_b</i>	<i>R_b</i>	<i>R_b</i>
SiO _x -5%	2.15	6.04	11.99	20.18
SiO _x -10%	1.78	6.94	7.27	15.99
SiO _x -15%	1.71	7.74	5.60	15.05
SiO _x -20%	2.15	4.29	4.89	11.34
SiO _x -25%	1.89	3.58	11.94	17.41
SiO _x -30%	1.62	3.39	8.24	13.25

Table 1. EIS results expressed as different ratio of SiO_x/C electrode

3.2. Physical characteristics

3.2.1. FT-IR results

The FT-IR was measured according to the AM and AA contents of P(AM-co-AA) copolymer. As depicted in Figure 10, the peak at 3450 cm^{-1} corresponds to the asymmetric stretching vibration of the amino group in acrylamide, while the peak at 3200 cm^{-1} represents the symmetric stretching vibration of the same group. The observed increase in binding energy of the amide peak, attributed to asymmetric stretching vibrations from polyacrylamide (PAM), can be explained by the space steric effect. This phenomenon is attributed to the interactions occurring between the amide group and various functional groups following the copolymerization process. Notably, the effect becomes increasingly pronounced with a rise in the acrylamide content. Furthermore, with an increase in the acrylamide ratio, the C=O peak of the copolymer becomes broader and more intense. This change is attributed to the enhanced hydrogen bonding interactions between the hydroxyl (-OH) groups and the carbonyl (C=O) groups.

3.2.2. Thermal analysis results

As shown Figure 11, DSC revealed the glass transition temperatures (T_g) of the polymer binder, with results indicating a T_g of $209.1\text{ }^\circ\text{C}$ for PAM, $237.8\text{ }^\circ\text{C}$ for a P(AM-AA)_{7:3}, $236.2\text{ }^\circ\text{C}$ for a P(AM-AA)_{5:5} and $213.7\text{ }^\circ\text{C}$ for a P(AM-AA)_{3:7}. Both the carboxyl and amide groups in these copolymers demonstrate stability across a broad temperature range, maintaining this stability up until the LIB reaches a temperature of $200\text{ }^\circ\text{C}$.

The weight change rate of the copolymer, as observed through TGA, is presented in Figure 12, based on these results. The decomposition of the copolymer, as indicated by the rapid mass loss curve, occurs in three distinct stages: at $98\text{ }^\circ\text{C}$, $240\text{ }^\circ\text{C}$, and $460\text{ }^\circ\text{C}$. In the initial stage, mass loss is attributed to the evaporation of moisture, while in the second stage, it is due to the formation of anhydride linkages between the carboxyl groups within the copolymer. The final stage of mass loss involves the decomposition of acrylic acid anhydride due to imidization and the release of ammonia. After the final step, copolymers with a high content of carboxyl groups exhibit less mass loss.

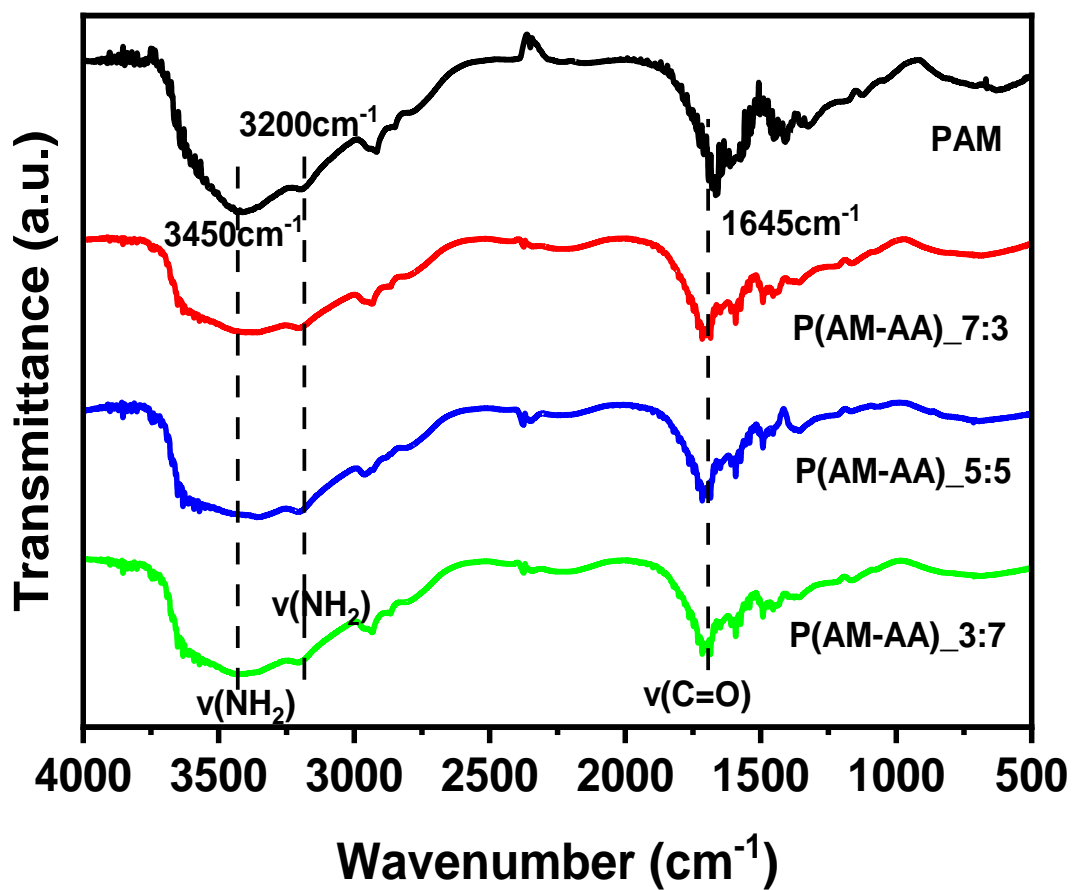


Figure 10. FT-IR results of different ratio of AA in P(AM-AA)

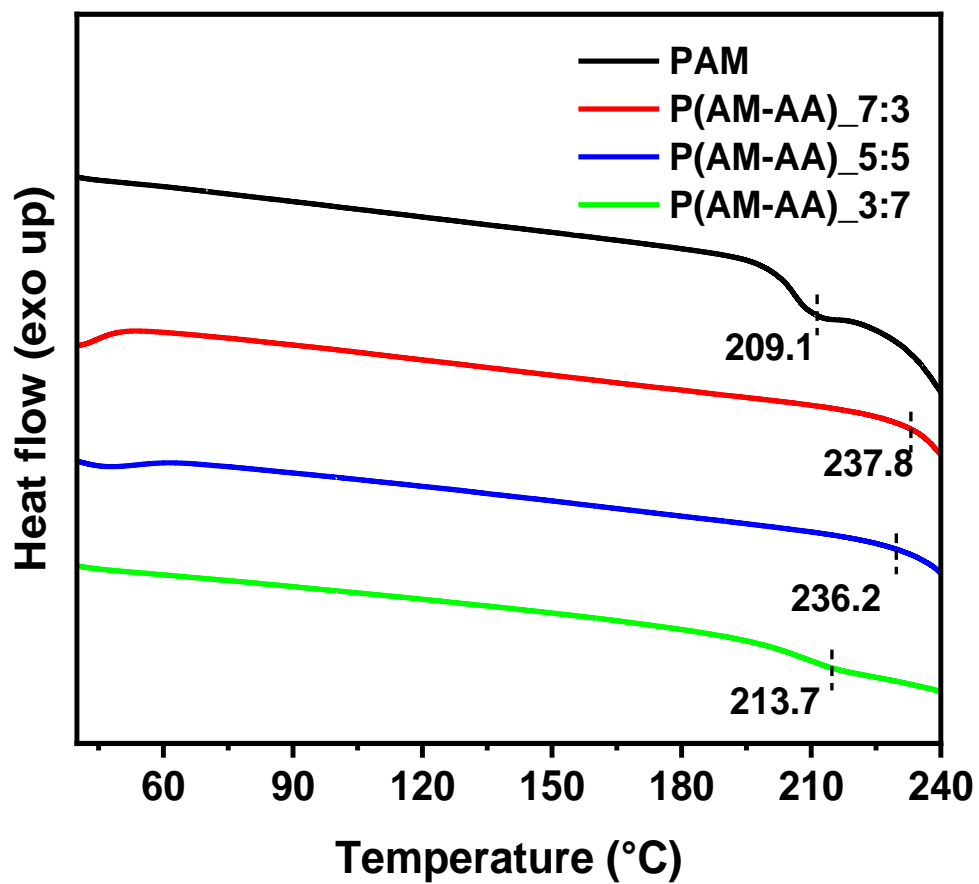


Figure 11. DSC results of different ratio of AA in P(AM-AA)

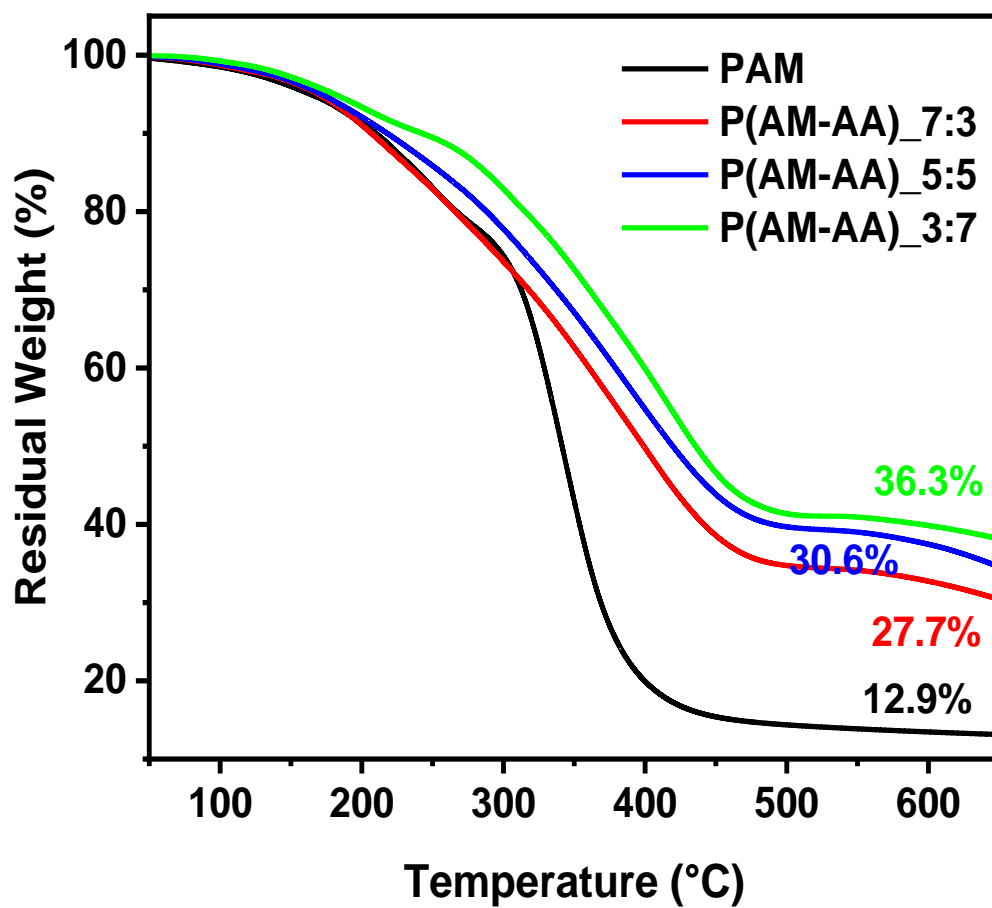


Figure 12. TGA results of different ratio of AA in P(AM-AA)

3.2.3. Rheological properties of binder and slurries results

To confirm the effect of the AM and AA monomer ratio on the rheological characteristics of both the pure P(AM-AA) binder and the P(AM-AA) binder in slurry, the ratio of AM and AA monomers in the slurry was varied. The ratios of the pure copolymer binder are shown in Figure 13. The P(AM-AA) 7:3 copolymer binder exhibited the highest viscosity in relation to shear rate, while still indicating that all binders displayed similar overall behavioral patterns. Finally, the same slurry viscosity was produced by adjusting the TSC of the slurry using distilled water.

The ratios of the copolymer binders in the slurry were changed to 7:3, 5:5, and 3:7. The rheological characteristics of the P(AM-AA) binder in slurry, measured and analyzed, are shown in Figure 14.

As a result, with an increase in the content of AA monomer, the slurry exhibits stronger shear thinning, as shown in Figure 14(a). Additionally, the results of the shear stress versus shear rate analysis, presented in Figure 14(b), reveal critical points where the slope of all slurries changes at shear rates ranging between 0.3 s^{-1} and 0.4 s^{-1} [55]. This indicates that the network structure among the particles within the slurry, which is maintained at a low shear rate and can be presumed to represent the slurry in a static state, disintegrates with increasing shear rates, leading to the formation of a new network structure. This phenomenon is indicative of the formation of a gel structure in the stationary slurry [56].

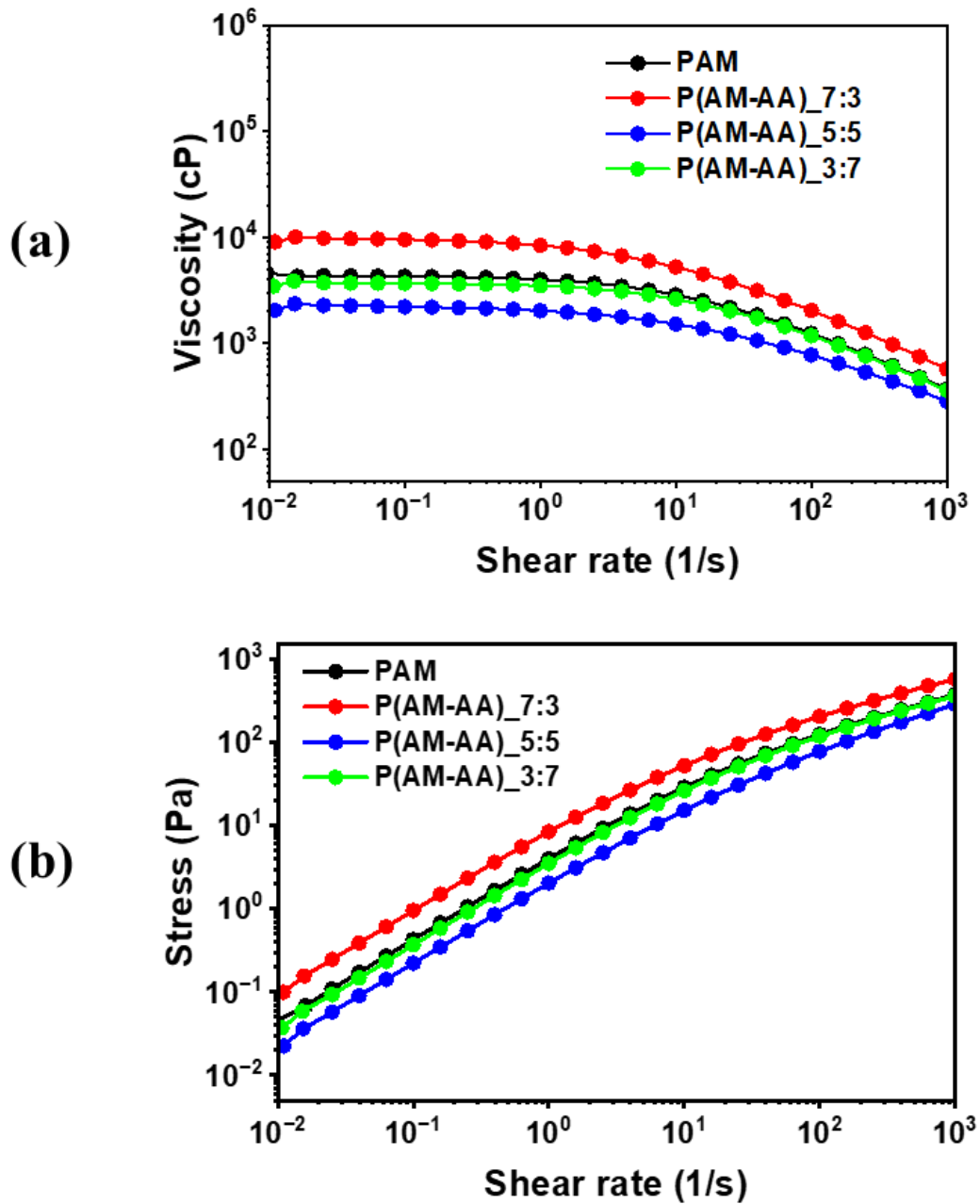


Figure 13. Rheological properties result of the pure binder (a) viscosity and (b) stress vs. shear rate depending on the ratio of AM and AA monomer

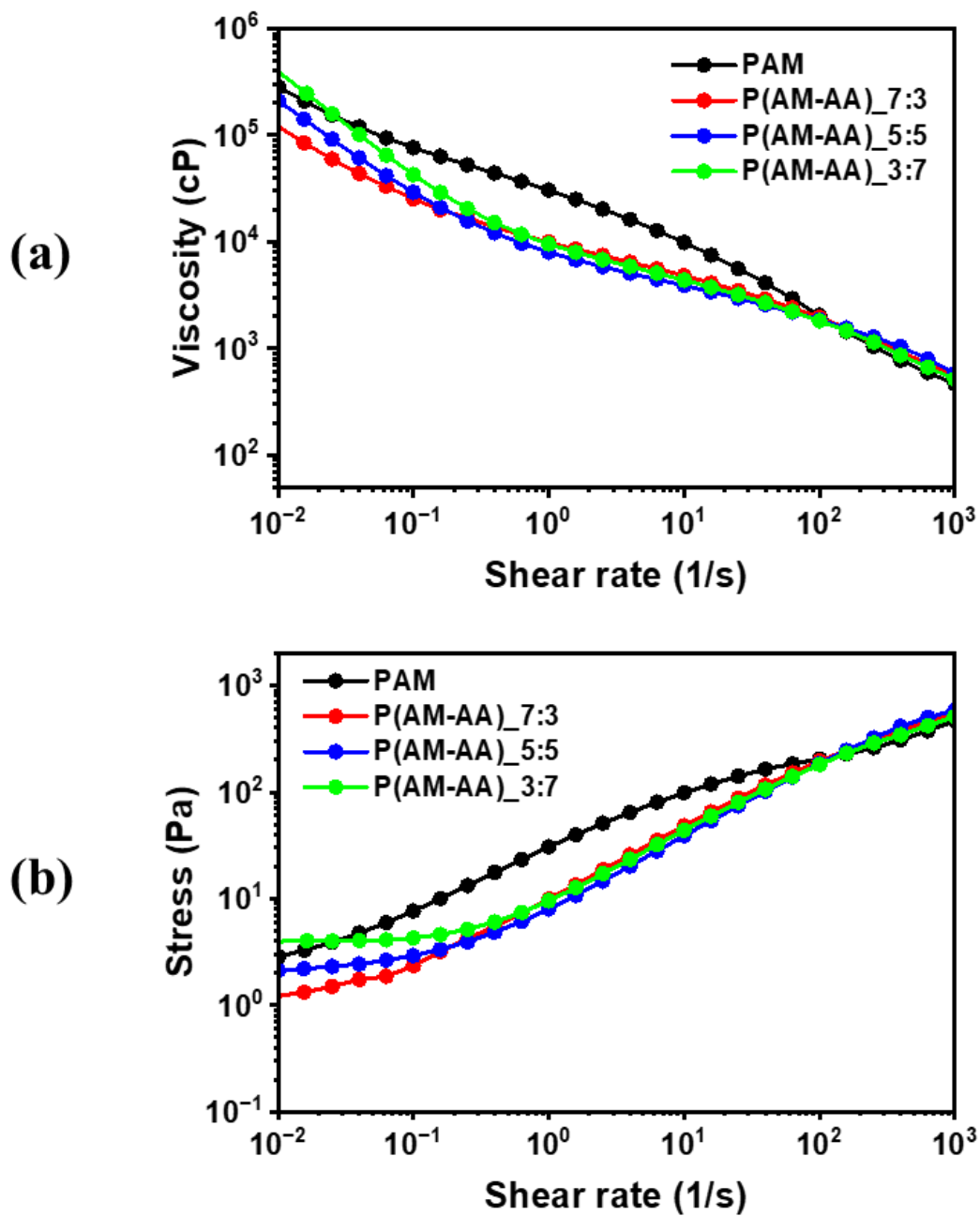


Figure 14. Rheological properties result of the (a) viscosity and (b) stress vs. shear rate depending on the ratio of AM and AA monomer in slurry

3.2.4. Electrode resistivity & resistance results

The comparatively low composite volumetric resistivity of the P(AM-AA)_{3:7} copolymer binder is shown in Figure 15. With the increase in AA monomer content, the carboxyl group of the AA monomer creates a covalent bond with the hydroxyl group on the SiO_x surface, possessing greater bonding energy compared to non-covalent hydrogen bonds. This enhances electronic conductivity and results in lower composite volumetric resistivity.

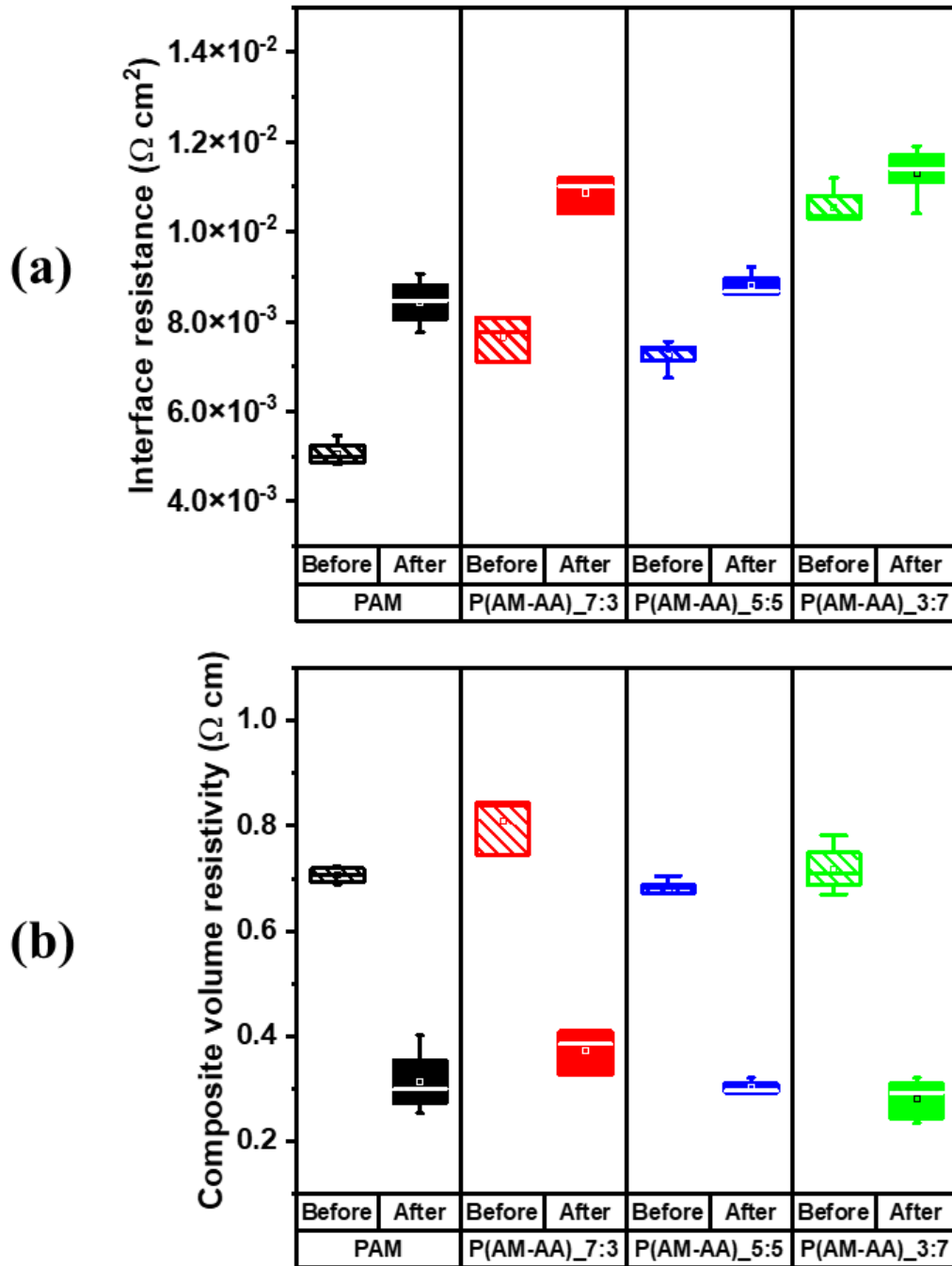


Figure 15. (a) Composite volume resistivity and (b) Interface resistance results of different ratio of AA in P(AM-AA)

3.2.5. Electrolyte uptake and adhesive strength results

The results of the electrolyte uptake analysis quantitatively demonstrate the capacity of the binder film to absorb and retain the electrolyte. The data on the electrolyte uptake of all binder samples are shown in Figure 16. After being immersed in the electrolyte for 14 hours, the electrolyte uptake of binders showed that PAM has approximately 13.5 % electrolyte uptake, which is relatively larger than other copolymer P(AM-AA) samples. However, the adhesion ability of the polymeric binder in the electrode is influenced by the amount of solvent uptake, which causes swelling of the binder. This swelling can potentially weaken the interaction between the active materials and the current collector compared to the poor adhesion of the PAM binder in Figure 17 may be partially attributed to the large electrolyte uptake [57]. The findings indicated that the relatively lower swelling capacity of the carbonate electrolyte in the binder might marginally reduce the ionic exchange of lithium ions through the SiO_x/C electrodes. However, this effect does not significantly impact the electrodes' high adhesive ability, which remains stable during long-term electrochemical reactions. Therefore, the P(AM-AA) _{7:3} ratio shows the highest adhesive strength due to electrolyte uptake, approximately 1.4 N.

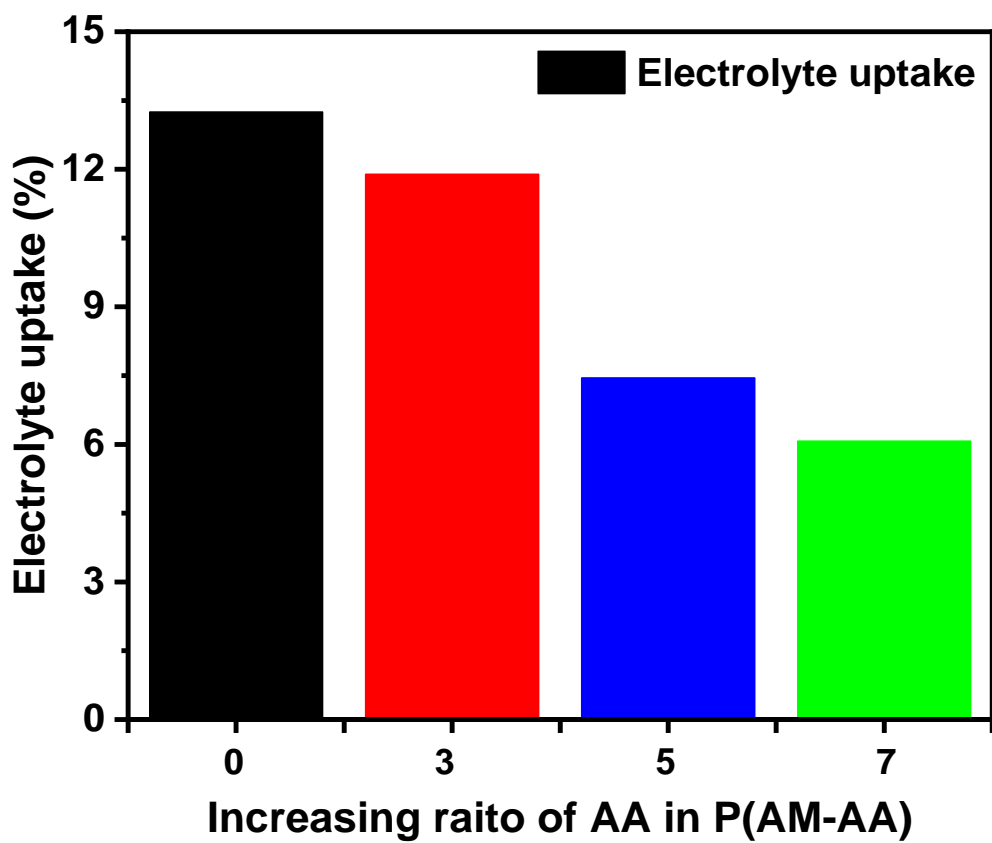


Figure 16. Electrolyte uptake results of different ratio of AA in P(AM-AA)

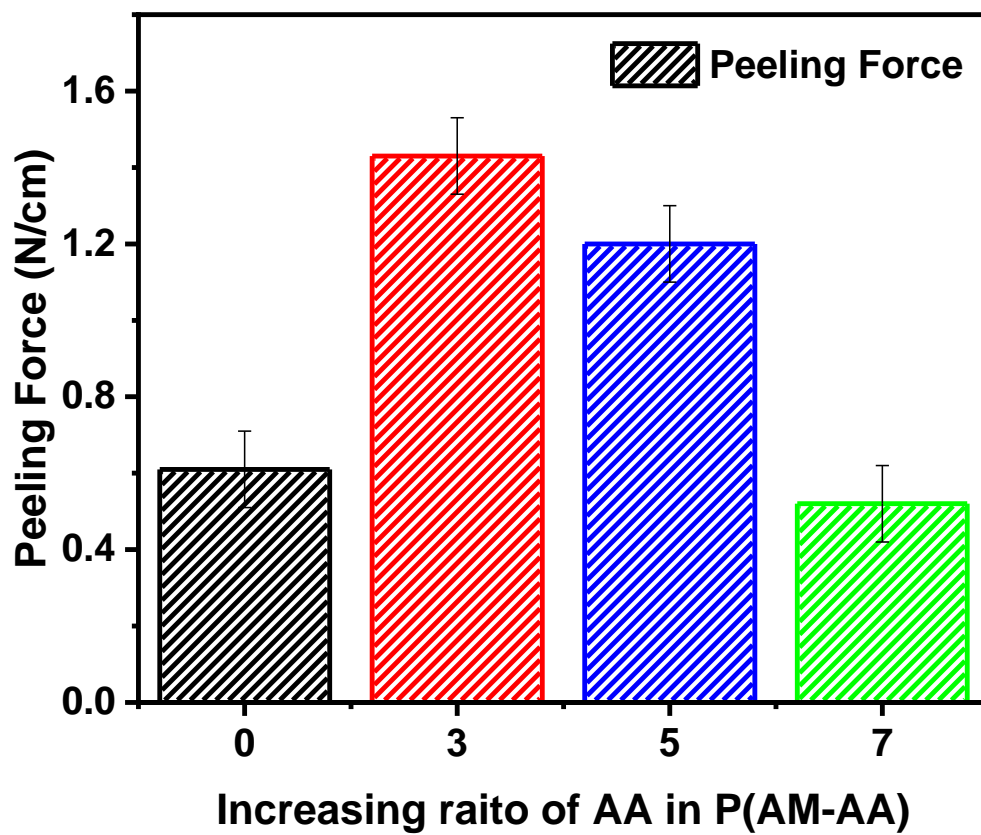


Figure 17. Average adhesive strength results of different ratio of AA in P(AM-AA)

3.3. Electrochemical characteristics

3.3.1. Cycle performance results

To evaluate the cycling performance of the copolymer binder in the SiO_x/C anode, especially in the context of volume expansion effects, a constant current charge-discharge test was conducted. This test was performed over 100 cycles at a current of 0.5C at 25 °C is shown in Figure 18.

The initial discharge capacities of PAM, 7:3, 5:5 and 3:7 anodes are 725.8, 713.8, 707.3, and 704.9 mAh/g, respectively, and the initial coulombic efficiency (ICE) is 79.0, 82.4, 82.0, 81.5 %, respectively. The ICE value increases with the increase in content of the amide groups, leading to the highest ICE value of the P(AM-co-AA) 7:3 anode. This observation indicates that the resilience resulting from hydrogen bonding interactions within the amide groups is essential for upholding the structural stability of the anode.

In the cycle performance, PAM demonstrates relatively superior cycle and rate characteristics; however, its capacity exhibits a rapid decline after 50 cycles. This phenomenon can be ascribed to the intrinsically lower bond strength of non-covalent hydrogen bonds compared to covalent bonds, which face challenges in adapting to the volumetric expansion of SiO_x. Consequently, P(AM-AA) 7:3 demonstrated superior cycle characteristics due to high adhesion.

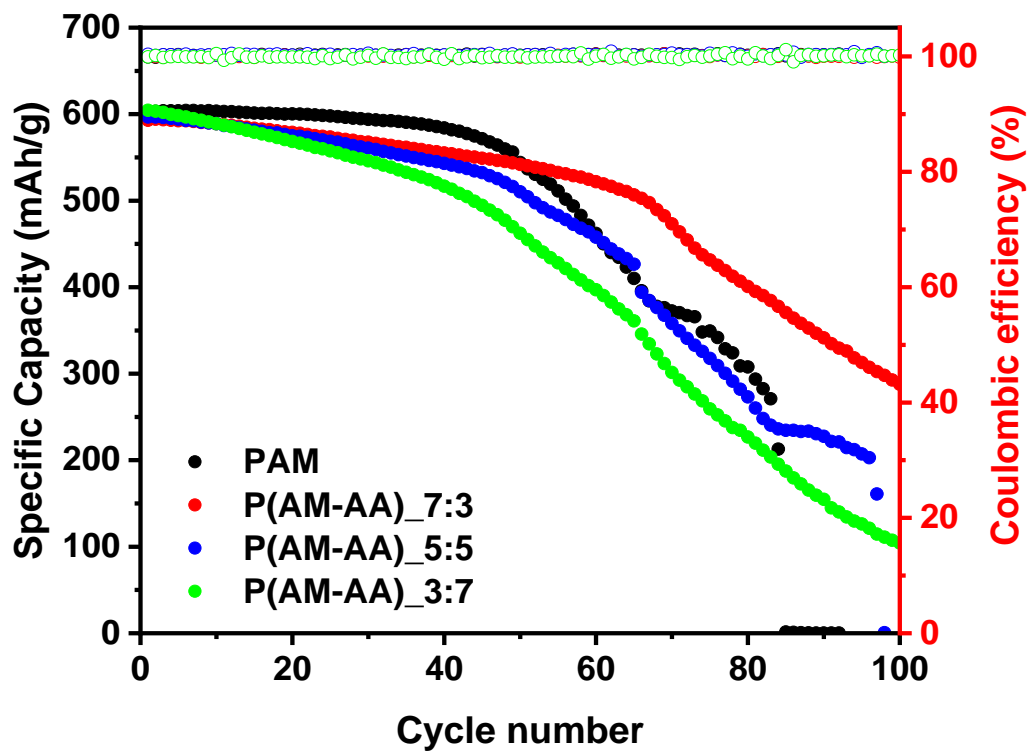


Figure 18. Cycling performance at 0.5C of different ratio of AA in P(AM-AA)

3.3.2. Rate capability results

Charge and discharge tests were conducted at currents of 0.1C, 0.2C, 0.5C, 1C, 2C, 5C, 10C, and 0.1C are shown in Figure 19. The results of the rate capability test indicated that with an increase in AM content, enhanced rate capability characteristics were observed. These results can be attributed to the fact that with an increase in acrylamide content, the polymer not only becomes harder due to an increase in partial covalent bonds but also exhibits a stretchable structure. It is also due to the increased hydrogen bonding between the hydroxyl group (-OH) and carbonyl group (C=O), which effectively accommodates the volume expansion of SiO_x, giving it excellent mechanical properties.

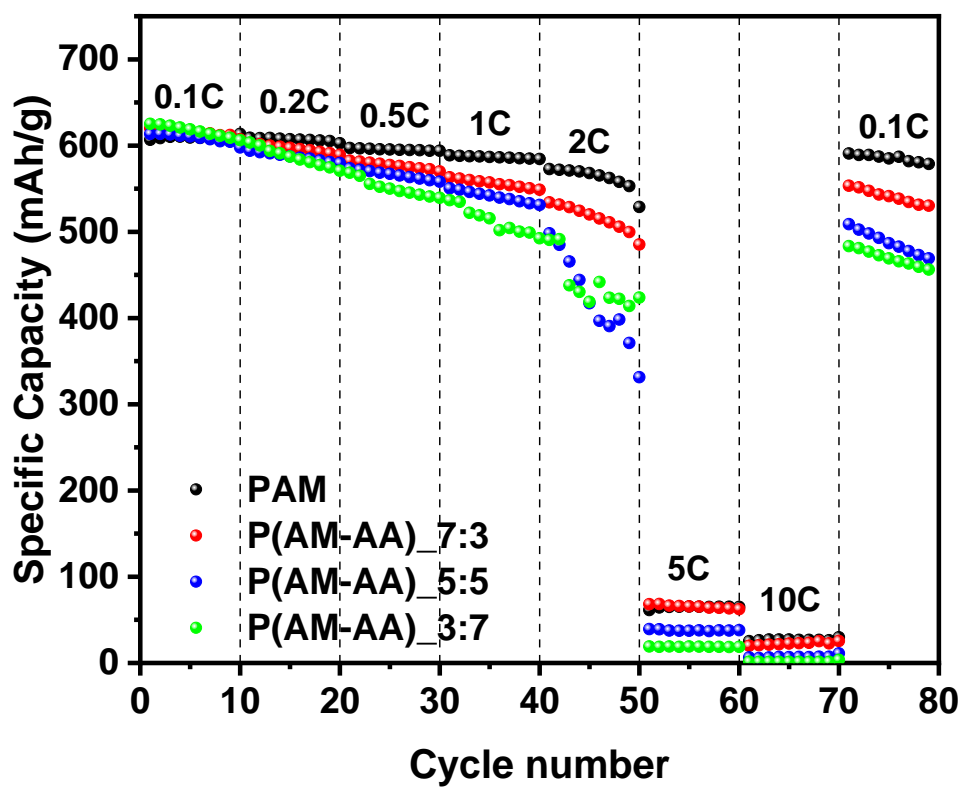


Figure 19. Rate capability at vs. C-rate with each 10 cycles of different ratio of AA in P(AM-AA)

3.3.3. Cyclic voltammetry results

The effect of copolymer P(AM-co-AA) binder on electrochemical properties of SiO_x/C anodes were conducted by CV, EIS, and galvanostatic cycle tests.

The electrochemical stability of the binder was confirmed through a Cyclic voltammetry (CV) test. CV measurements were conducted on the SiO_x/C electrode within a range of 0.005 V to 3.0 V at a sweep rate of 0.2 mV/s after 2 cycles. As depicted in Figure 20, the copolymer P(AM-AA) exhibited a significantly larger current peak compared to PAM. The two broad peaks around 0.36 and 0.57 V correspond to the delithiation process of the Li-Si alloy [58]. In addition, the observed gradual increase in peak intensity at 0.1 V, as the cycling process progresses, is indicative of the electrolyte's penetration into the electrodes and the ensuing electrochemical activation of SiO_x/C anode electrode.

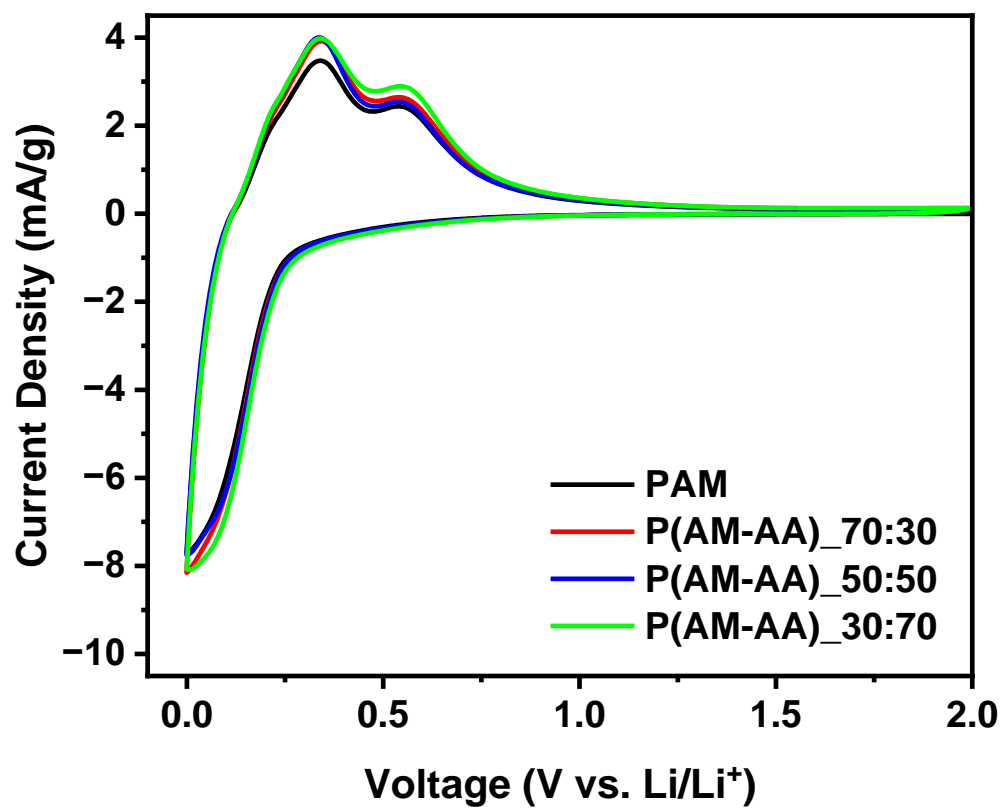


Figure 20. CV curve results of different ratio of AA in P(AM-AA)

3.3.4. Electrochemical Impedance Spectroscopy results

The EIS of the SiO_x/C electrodes was measured at 0.2 V after two pre-cycles at 0.1C followed by two more cycles at 0.5C. EIS results are shown in Figure 21. The semicircles observed in the middle frequency range are indicative of the charge transfer resistance associated with the electrochemical reactions at the interface, which are fundamentally linked to the ion and electron transport characteristics. Remarkably, the P(AM-AA) _{3:7} copolymer binder exhibits the lowest charge transfer resistance. The observed phenomenon is attributed to the enhanced electron transfer between the electrolyte and the electrode due to an increase in AA monomer content, similar to the patterns noted in the electrode resistance and CV graph.

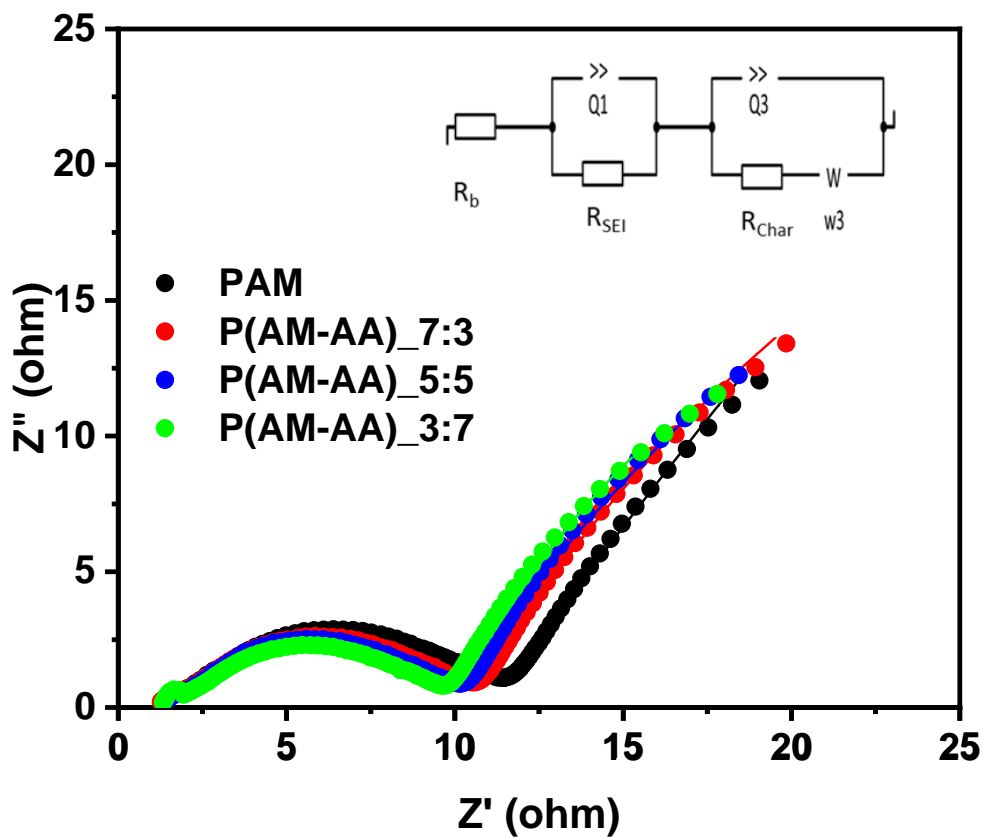


Figure 21. EIS results expressed as different ratio of AA in P(AM-AA)

SiO _x /C electrode	Resistance, R (Ω)			
	R_b	R_{SEI}	R_{char}	R
PAM	1.21	1.55	10.87	13.63
P(AM-AA)_7:3	1.33	0.98	10.04	12.35
P(AM-AA)_5:5	1.23	0.75	9.18	11.16
P(AM-AA)_3:7	1.28	0.83	6.45	8.56

Table 2. EIS results expressed as different ratio of AA in P(AM-AA)

3.3.5. Thickness change results after cycling

The degree of volume expansion of SiO_x, as indicated by the change in thickness of the electrode before and after 100 cycles, influenced by the effect of the copolymer binder, is shown in Figure 22. The thickness change was largest in P(AA-AA)_{3:7} copolymer binder, and the thickness change gradually decreased as the content of the amide group increased. This indicates a significant volume change, as the weaker strength of non-covalent hydrogen bonds, compared to covalent bonds, makes it difficult to manage the expansion of SiO_x.

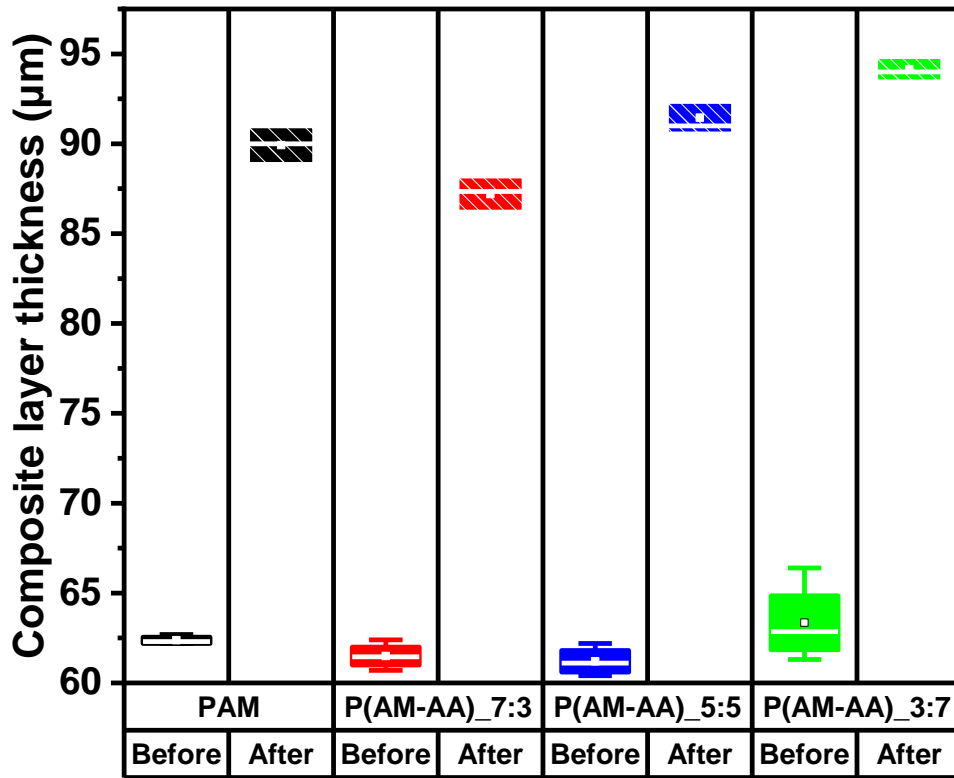


Figure 22. Thickness change results after 100 cycles expressed as different ratio of AA in P(AM-AA)

3.4 Conclusion

The copolymer P(AM-AA) was synthesized via free radical polymerization, utilizing acrylamide (AM) and acrylic acid (AA) monomers, which are abundant in amide and hydroxyl groups. As the content of AA monomer in the copolymer binder increased, low charge transfer resistance and excellent CV peak value were confirmed. However, it showed low cycle performance due to low adhesion. Therefore, P(AM-co-AA)_{7:3}, which had the highest adhesion, showed the best cycle performance. In conclusion, as the AA monomer content increased, the volume expansion of SiO_x was suppressed due to the increase in covalent bonds forming a rigid 3D network. However, due to low elasticity and irreversible interactions, the capacity during lithiation/delithiation of the cycle decreased dramatically. On the other hand, as the AM monomer content increases will form hydrogen bonds with the hydroxyl groups. Non-covalent bonding is the basis for the elastic force in the binder. Therefore, it can be explained by the synergistic effect between the covalent bond formed through dehydration condensation reaction of the hydroxyl group of AA and SiO_x, and the non-covalent bond resulting from the hydrogen bond between AM and the hydroxyl group on the SiO_x surface. It helps to mitigate the volume expansion of high-capacity SiO_x/C anode electrodes. Such interactions significantly contribute to the excellent mechanical stability and electrochemical performance of SiO_x/C anode electrode.

4. Results and discussion

4.1. Physical characteristics

4.1.1. Optimal ratio of conductive materials

Prior to the binder comparative evaluation experiment, we first conducted an experiment to determine the optimal ratio of active materials and conductive materials. The optimal ratio for all materials, excluding the binder, is shown in Figure 23. As a result of using 1/5/10 wt% of MWCNT conductive material, capacity at 1C was achieved starting from 10 wt%, as shown in Figure 23 (a).

As a result of using 20/30 wt% of Super P, capacity at 1C was achieved starting from 30 wt%, as shown in Figure 23 (b). When MWCNTs were used, capacity was achieved even with a relatively small amount due to their high electronic conductivity, but they exhibited low dispersibility.

Conversely, while Super P demonstrated good dispersibility, controlling the electrode's thickness and the loading level was challenging due to the necessity of using a large amount. Therefore, in order to complement the characteristics of the two materials, we physically mixed MWCNT and Super P to find the optimal ratio.

The superior rate capability at the target loading level was confirmed in Figure 23 (c) when a composite conductive material with a Super P + MWCNT ratio of 15 wt% + 5 wt% was used.

We conducted a binder comparative evaluation experiment using this specific ratio.

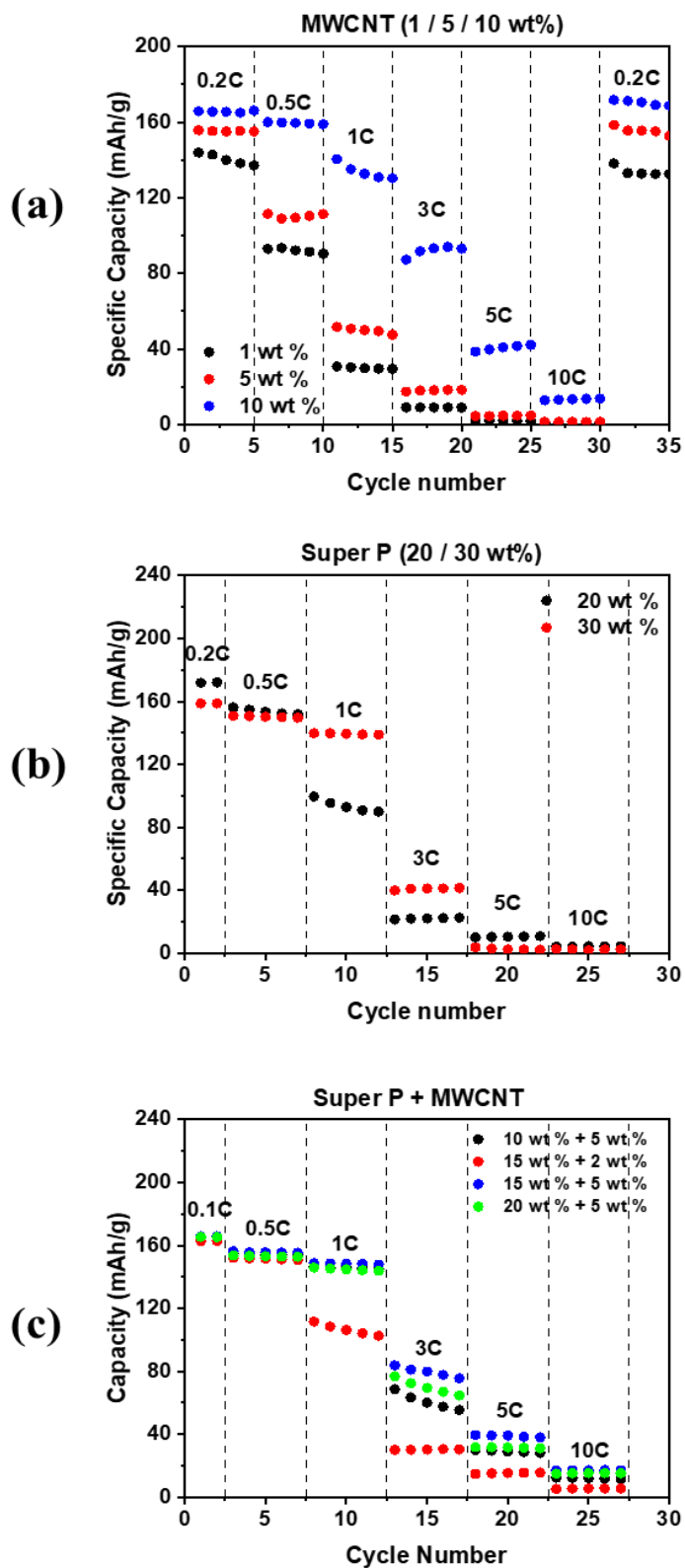


Figure 23. (a) MWCNT (b) Super P and (c) physical mixing of both MWCNT and Super P at C-rate with each 5 cycles and voltage range from 2.7 V to 4.2 V in solvent-free dry electrode.

4.1.2. Electrode resistivity and resistance results

Figure 24 shows that interfacial resistance and composite volume resistivity tend to decrease as the PVDF content increases. This shows that PVDF has excellent surface dispersion power in the NCM and Al current collectors, and there is no chemical reaction between the surfaces of the battery materials, which increases the overall bonding force [59]. Furthermore, it is observed that, compared to the PTFE polymer binder, the electrode resistance is lower due to the inherently low resistance of the PVDF polymer.

4.1.3. Adhesive strength results

The PTFE polymer, due to its fibrous characteristics, undergoes elongation at a temperature of approximately 19 °C during the kneading process. Subsequently, the self-supporting dry electrode is shaped by a rolling process between rollers at a high temperature of about 110 °C using a 3-roll mill. A 180° peel test was performed to evaluate the adhesion of the active material including the binder and current collector and the conductive material. Superior adhesion with increasing PTFE content is shown in Figure 25. With an increase in the PTFE polymer binder content, the self-supporting structure of the electrode is more strongly maintained, owing to enhanced stretchability within the electrode.

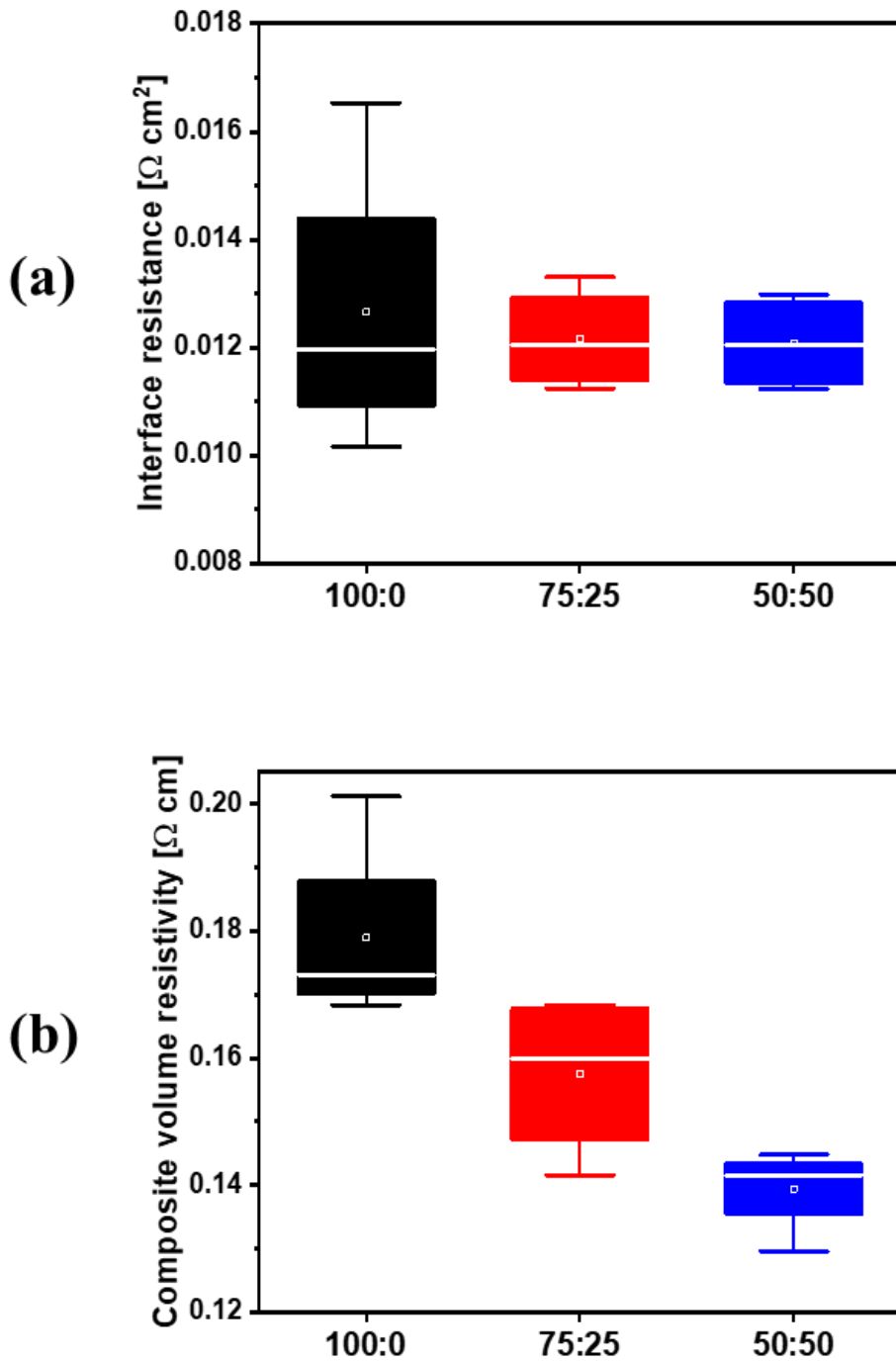


Figure 24. (a) Interface resistance and (b) composite volume resistivity results of different ratio of PTFE and PVDF binder in solvent-free dry electrode

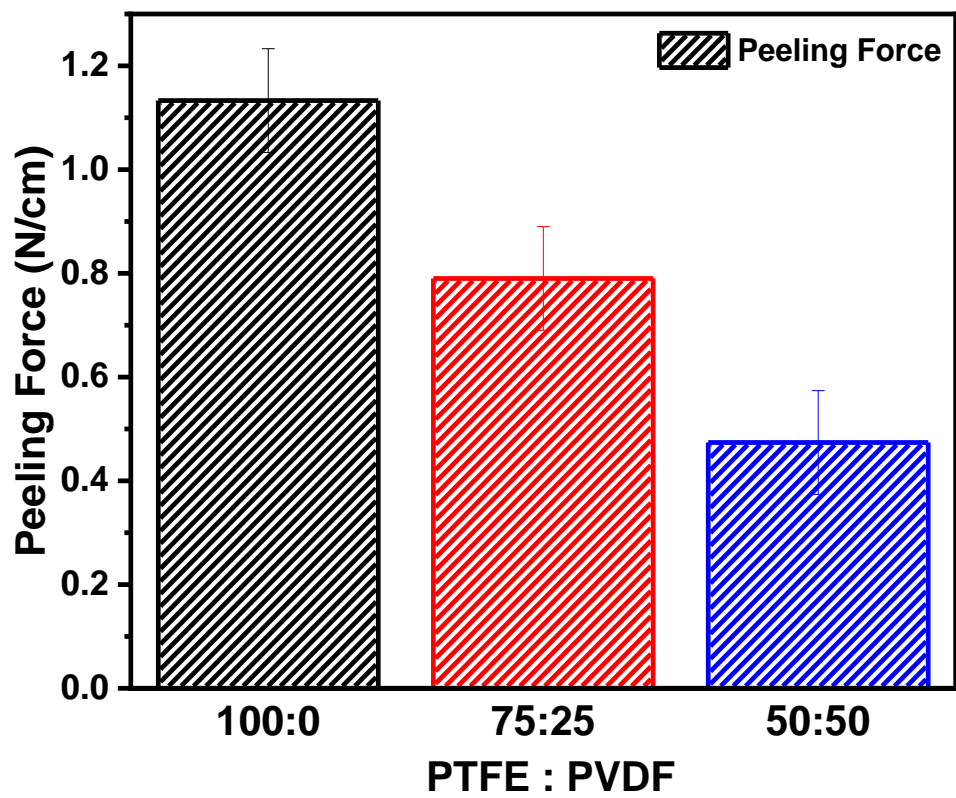


Figure 25. Average adhesive strength results of different ratio of PTFE and PVDF binder in solvent-free dry electrode

4.1.4. Surface and Interfacial Cutting and Analysis System results

The 180° peel test shows that the adhesion strength, as indicated by these tests, is primarily due to surface adhesion properties, rather than the bulk material or the interface between the electrode composite and current collector. It affects the ability to obtain specific adhesion strength at certain locations, such as the interface between the electrode composite and current collector, or the internal cohesion at a point within the electrode composite. SAICAS can overcome this limitation [60].

As a result, it showed a similar tendency to the 180° peeling test. Figure 26 shows that with an increase in PTFE content, the adhesion between the current collector and the active material is enhanced. In dry electrodes, a homogeneous distribution of the binder throughout the electrode is indicated, contrasting with the heterogeneous binder distribution resulting from the capillary force during the drying process in the wet method.

4.1.5. FE-SEM results

The PTFE fibrils could be observed on the surface of the lithiated NCM622 dry electrode in SEM images, as shown in Figure 27. PTFE fibrils tie up NCM622 particles, creating a dense and compact structure.

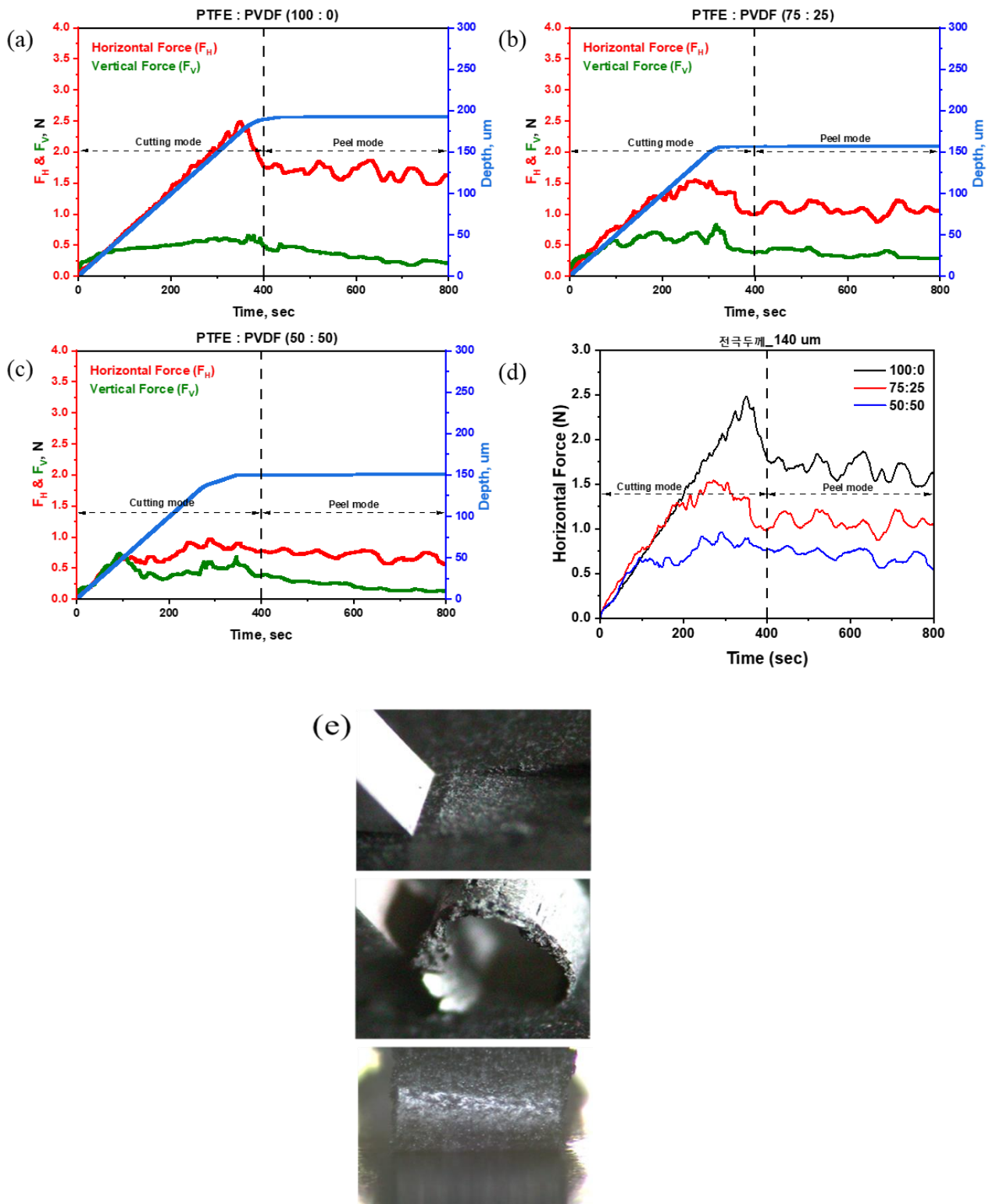


Figure 26. (a) 100:0 (b) 75:25 (c) 50:50 (d) average horizontal force and (e) SAICAS images of different ratio of PTFE and PVDF binder in solvent-free dry electrode

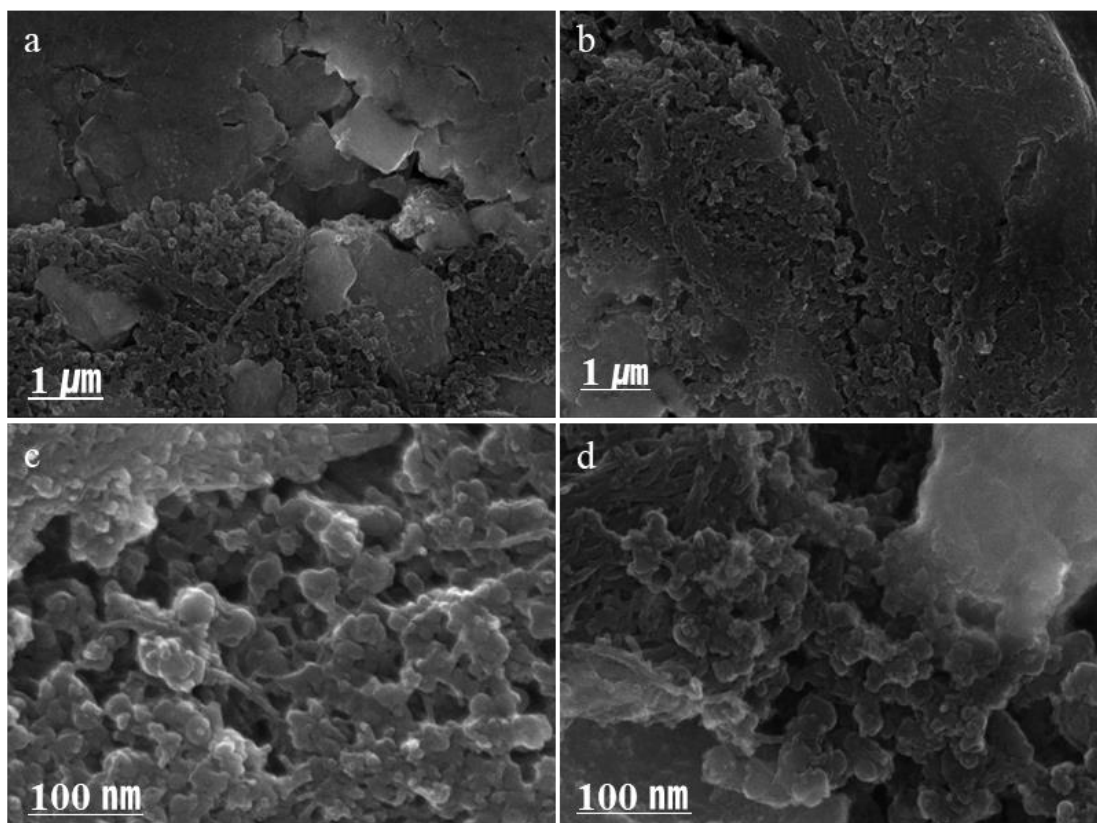


Figure 27. FE-SEM images PTFE fibrilization of solvent-free dry electrode with different magnification: (a) 20,000x, (b) 25,000x, (c) 100,000x and (d) 100,000x

4.2. Electrochemical characteristics

4.2.1. Cycle performance and rate capability results

Galvanostatic charge-discharge tests were performed to evaluate the cycling performance of the high-loading cathode solvent-free electrode. This test was performed over 200 cycles at a current of 1C at 25 °C is shown in Figure 28.

PTFE polymers exhibit higher resistance compared to PVDF polymers. Therefore, even though the 100:0 ratio exhibited the strongest adhesion, its cycle performance was comparatively lower. On the contrary, with an increase in PVDF content, a decrease in resistance is observed, and improved performance is evident through electrochemical analyses, including C-rate, cyclic voltammetry (CV) curves, and electrochemical impedance spectroscopy (EIS). As a result, the PTFE:PVDF ratio of 75:25 exhibits superior cycling characteristics compared to the 50:50 ratio, due to its higher adhesion strength. This primarily occurs due to inadequate fiber formation, hindering the development of a solvent-free dry electrode. In conclusion, the reduced adhesion can lead to the detachment of the positive active material from the current collector during cycling, which contributes to a decline in capacity. These outcomes are evident in the swift reduction in capacity following 100 cycles.

The rate capability of solvent-free dry electrodes containing different ratio of PTFE and PVDF binders was tested in the range of 2.7 V to 4.2 V and the current changes for every 5 cycles from 0.2C to 10C with the final cycles returning to the current rate of 0.2C is shown in Figure 29.

As a result of the rate capability test, enhanced rate performance characteristics were observed with the increasing content of PVDF. It was due to better transfer of lithium ions from low resistance, like what was seen in the cycle test.

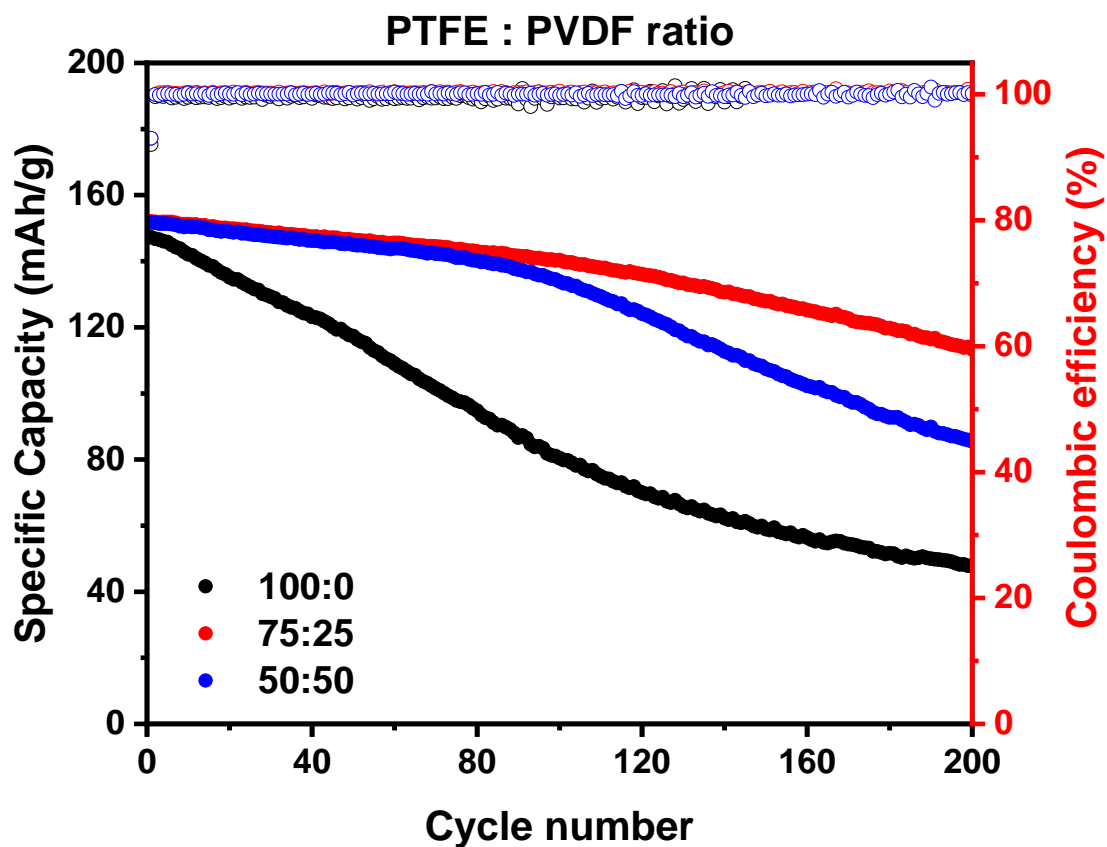


Figure 28. Cycling performance at 1C of different of PTFE and PVDF binder in solvent-free dry electrode

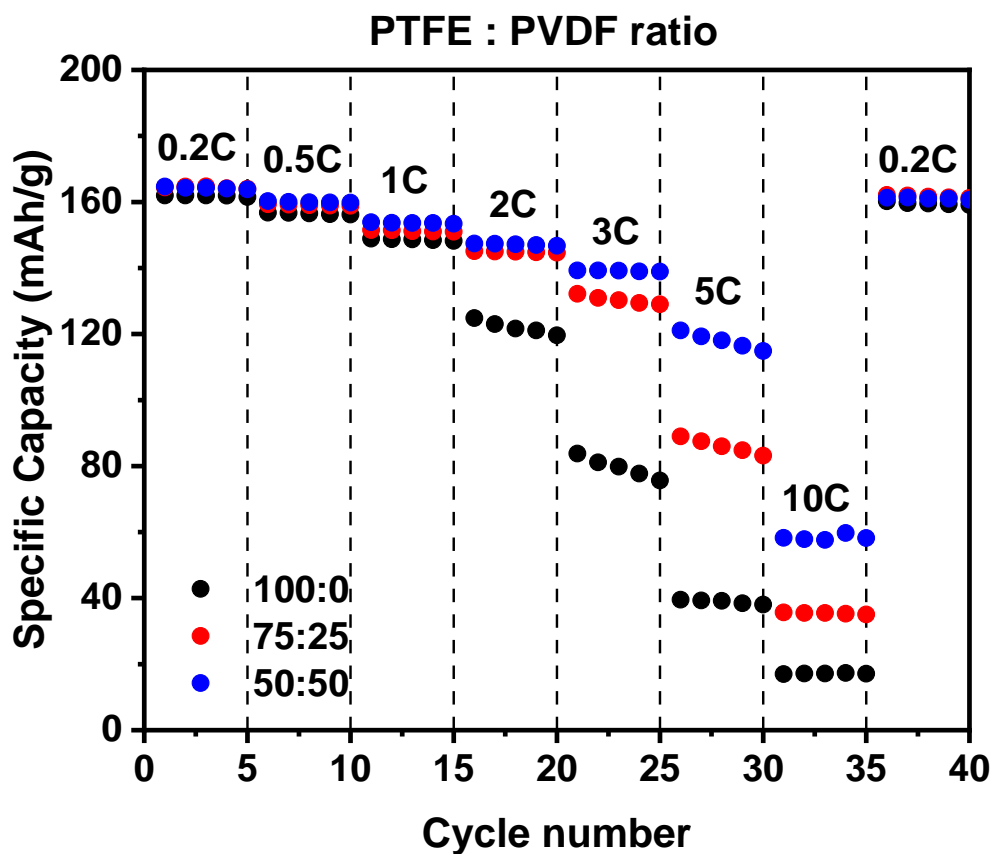


Figure 29. Rate capability at vs. C-rate with each 5 cycles of different of PTFE and PVDF binder in solvent-free dry electrode

4.2.2. Cyclic voltammetry results

To clarify the influence of binders on the charge-discharge processes of solvent-free dry electrodes, CV tests were performed at a sweep rate of 0.2 mV/s for three cycles and the voltage range from 2.7 V to 4.2 V are shown in Figure 30.

The tailing of the oxidation peak in Figure 30 (a) indicates that the oxidation reaction persists beyond 4.2 V, demonstrating unstable characteristics. Conversely, with an increase in PVDF content, a stable redox peak size is observed. The PVDF polymer binder not only exhibits low resistance, but also possesses superior surface dispersion and does not undergo any surface chemical reaction with the Al current collector in the NCM cathode active material, leading to outstanding overall bonding strength.

The potential interval value is frequently used to evaluate the polarization of electrode materials [61]. As a result, the PTFE:PVDF ratio of 50:50 had the lowest potential interval value of 0.3143 V, indicating that less polarization occurred. This reduces the length of the lithium diffusion path, and a similarity can be observed with the excellent electrochemical performance demonstrated in previous electrode resistance, cycling tests, and rate capability tests.

4.2.3. Electrochemical Impedance Spectroscopy results

The EIS of the SiO_x/C electrodes was measured at 0.2 V after two pre-cycles at 0.2C followed by two more cycles at 1C. EIS results are shown in Figure 31. The semicircles observed in the middle frequency range are indicative of the charge transfer resistance associated with the electrochemical reactions at the interface, which are fundamentally linked to the ion and electron transport characteristics. Remarkably, a binder with a PTFE:PVDF ratio of 50:50 exhibits the highest charge transfer resistance. The phenomenon observed can be attributed to a decrease in electron transfer between the electrolyte and the electrode, a consequence of the electrode's limited adhesion capability.

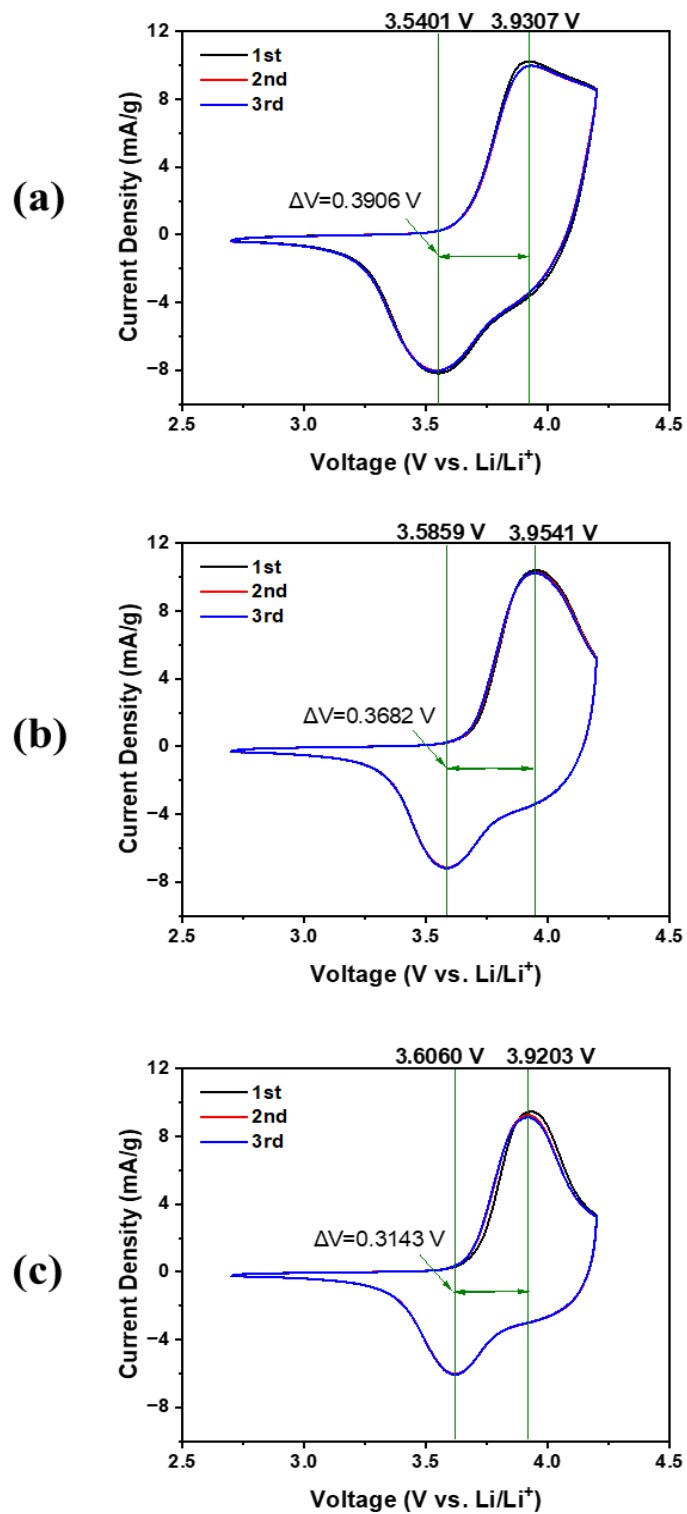


Figure 30. (a) 100:0 (b) 75:25 and (c) 50:50 CV curves of different ratio of PTFE and PVDF binder in solvent-free dry electrode

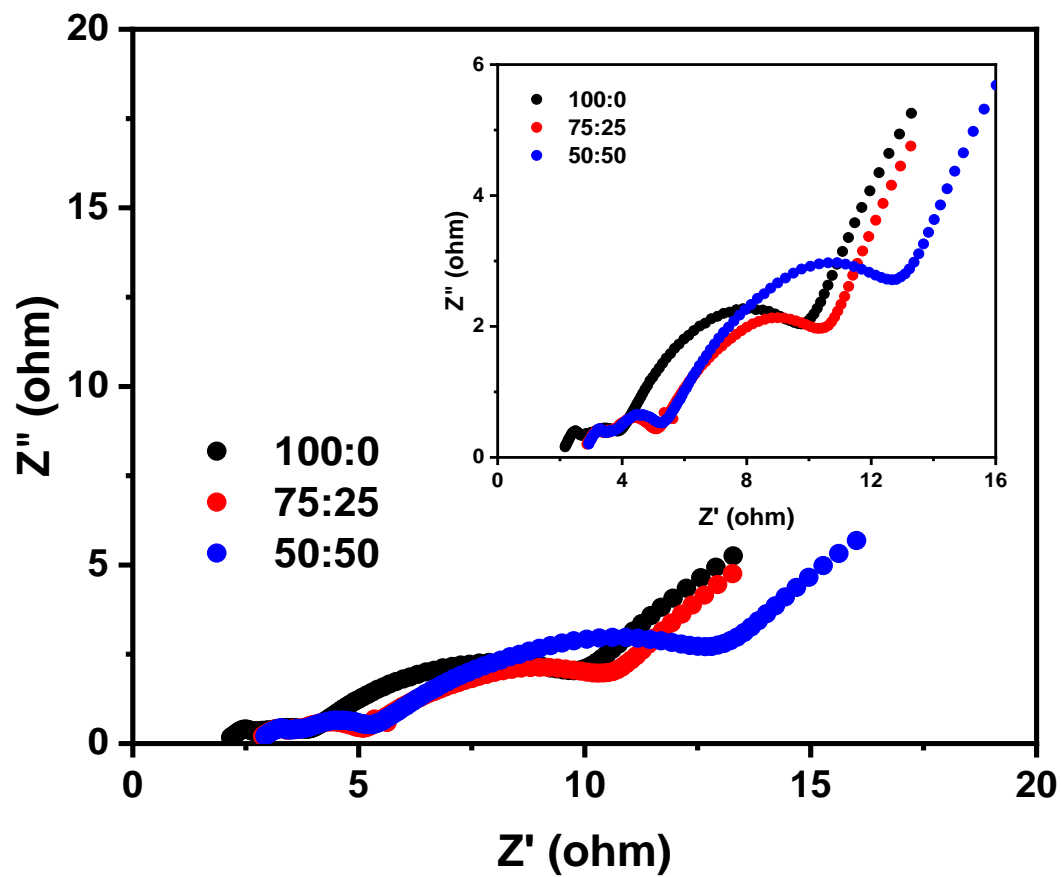


Figure 31. EIS results expressed as different ratio of PTFE and PVDF binder in solvent-free dry electrode

4.3 Conclusion

In this work, we successfully fabricated a solvent-free cathode electrode with a loading level of 19 mg/cm^2 by producing a free-standing dry electrode. This was achieved without using any solvent, through the fibrilization of the PTFE polymer binder in the battery electrode manufacturing method. We conducted evaluations of physical and electrochemical properties based on the ratio of the PVDF polymer binder used in the conventional wet process and the PTFE polymer binder, which aids in the manufacturing of self-supporting electrodes through polymer fibrilization.

Consequently, with an increase in PTFE binder content, a higher adhesion was observed, attributed to the strong fibrilization within the electrode. It contributes strong mechanical strength to the electrode. On the other hand, with an increase in PVDF binder content, the electrode exhibited lower electrode resistance, owing to the inherently lower resistance of this polymer compared to the PTFE polymer binder. In addition, the PVDF polymer binder not only exhibits low resistance, but also possesses superior surface dispersion and does not undergo any surface chemical reaction with the Al current collector in the NCM cathode active material, leading to outstanding overall bonding strength. As a result, superior electrochemical outcomes were achieved, as evidenced by rate capability tests, CV curves, and EIS. However, due to low adhesion, it was confirmed that the electrode with a PTFE:PVDF ratio of 75:25 had better cycle performance compared to 50:50 after 100 cycles.

Through this research, it was determined that the fibrilization PTFE polymer binder preserves the shape of the free-standing dry electrode and imparts mechanical strength to it. Additionally, this method can be easily integrated into the existing commercial roll-to-roll production line, showcasing significant potential for mass production, and promising to replace the current slurry casting procedure for commercial LIBs.

5. Reference

- [1] Li, M., Lu, J., Chen, Z., & Amine, K. (2018). 30 years of lithium-ion batteries. *Advanced Materials*, 30(33), 1800561.
- [2] Whittingham, M. S. (2004). Lithium batteries and cathode materials. *Chemical reviews*, 104(10), 4271-4302.
- [3] Zeng, X., Li, J., & Singh, N. (2014). Recycling of spent lithium-ion battery: a critical review. *Critical Reviews in Environmental Science and Technology*, 44(10), 1129-1165.
- [4] Blomgren, G. E. (2016). The development and future of lithium ion batteries. *Journal of The Electrochemical Society*, 164(1), A5019.
- [5] Manthiram, A. (2017). An outlook on lithium ion battery technology. *ACS central science*, 3(10), 1063-1069.
- [6] Ma, S., Jiang, M., Tao, P., Song, C., Wu, J., Wang, J., ... & Shang, W. (2018). Temperature effect and thermal impact in lithium-ion batteries: A review. *Progress in Natural Science: Materials International*, 28(6), 653-666.
- [7] Tomaszewska, A., Chu, Z., Feng, X., O'kane, S., Liu, X., Chen, J., ... & Wu, B. (2019). Lithium-ion battery fast charging: A review. *ETransportation*, 1, 100011. Tomaszewska, A., Chu, Z., Feng, X., O'kane, S., Liu, X., Chen, J., ... & Wu, B. (2019). Lithium-ion battery fast charging: A review. *ETransportation*, 1, 100011
- [8] Qi, W., Shapter, J. G., Wu, Q., Yin, T., Gao, G., & Cui, D. (2017). Nanostructured anode materials for lithium-ion batteries: principle, recent progress and future perspectives. *Journal of Materials Chemistry A*, 5(37), 19521-19540.
- [9] Goodenough, J. B., & Park, K. S. (2013). The Li-ion rechargeable battery: a perspective. *Journal of the American Chemical Society*, 135(4), 1167-1176.
- [10] Whittingham, M. S. (2014). Ultimate limits to intercalation reactions for lithium batteries. *Chemical reviews*, 114(23), 11414-11443.
- [11] Wood, D. L., Li, J., & An, S. J. (2019). Formation challenges of lithium-ion battery manufacturing. *Joule*, 3(12), 2884-2888.
- [12] Goodenough, J. B. (2018). How we made the Li-ion rechargeable battery. *Nature Electronics*, 1(3), 204-204.
- [13] Reynolds, C. D., Slater, P. R., Hare, S. D., Simmons, M. J., & Kendrick, E. (2021). A review of metrology in lithium-ion electrode coating processes. *Materials & Design*, 209, 109971.

- [14] Duffner, F., Mauler, L., Wentker, M., Leker, J., & Winter, M. (2021). Large-scale automotive battery cell manufacturing: Analyzing strategic and operational effects on manufacturing costs. *International Journal of Production Economics*, 232, 107982.
- [15] Schmitt, M., Baunach, M., Wengeler, L., Peters, K., Junges, P., Scharfer, P., & Schabel, W. (2013). Slot-die processing of lithium-ion battery electrodes—Coating window characterization. *Chemical Engineering and Processing: Process Intensification*, 68, 32-37.
- [16] Wenzel, V., Nirschl, H., & Nötzel, D. (2015). Challenges in lithium-ion-battery slurry preparation and potential of modifying electrode structures by different mixing processes. *Energy Technology*, 3(7), 692-698.
- [17] Baunach, M., Jaiser, S., Schmelzle, S., Nirschl, H., Scharfer, P., & Schabel, W. (2016). Delamination behavior of lithium-ion battery anodes: Influence of drying temperature during electrode processing. *Drying technology*, 34(4), 462-473.
- [18] Wood III, D. L., Li, J., & Daniel, C. (2015). Prospects for reducing the processing cost of lithium ion batteries. *Journal of Power Sources*, 275, 234-242.
- [19] Ahmed, S., Nelson, P. A., Gallagher, K. G., & Dees, D. W. (2016). Energy impact of cathode drying and solvent recovery during lithium-ion battery manufacturing. *Journal of Power Sources*, 322, 169-178.
- [20] Väyrynen, A., & Salminen, J. (2012). Lithium ion battery production. *The Journal of Chemical Thermodynamics*, 46, 80-85.
- [21] Wolter, M., Leiva, D., Fritsch, M., & Börner, S. (2013, November). Process development and optimization for Li-ion battery production. In *2013 World Electric Vehicle Symposium and Exhibition (EVS27)* (pp. 1-5). IEEE.
- [22] Hawley, W. B., & Li, J. (2019). Electrode manufacturing for lithium-ion batteries—Analysis of current and next generation processing. *Journal of Energy Storage*, 25, 100862.
- [23] Ludwig, B., Zheng, Z., Shou, W., Wang, Y., & Pan, H. (2016). Solvent-free manufacturing of electrodes for lithium-ion batteries. *Scientific reports*, 6(1), 23150.
- [24] Park, D. W., Cañas, N. A., Wagner, N., & Friedrich, K. A. (2016). Novel solvent-free direct coating process for battery electrodes and their electrochemical performance. *Journal of Power Sources*, 306, 758-763.
- [25] Jin, Y., Zhu, B., Lu, Z., Liu, N., & Zhu, J. (2017). Challenges and recent progress in the development of Si anodes for lithium-ion battery. *Advanced Energy Materials*, 7(23), 1700715.
- [26] Zhang, Y., Lu, S., Wang, Z., Volkov, V., Lou, F., & Yu, Z. (2023). Recent technology development in solvent-free electrode fabrication for lithium-ion batteries. *Renewable and Sustainable Energy Reviews*, 183, 113515.

- [27] Verdier, N., Foran, G., Lepage, D., Prébé, A., Aymé-Perrot, D., & Dollé, M. (2021). Challenges in solvent-free methods for manufacturing electrodes and electrolytes for lithium-based batteries. *Polymers*, 13(3), 323.
- [28] Ryu, M., Hong, Y. K., Lee, S. Y., & Park, J. H. (2023). Ultrahigh loading dry-process for solvent-free lithium-ion battery electrode fabrication. *Nature Communications*, 14(1), 1316.
- [29] Liu, Y., Gong, X., Podder, C., Wang, F., Li, Z., Liu, J., ... & Wang, Y. (2023). Roll-to-roll solvent-free manufactured electrodes for fast-charging batteries. *Joule*, 7(5), 952-970.
- [30] Ludwig, B., Zheng, Z., Shou, W., Wang, Y., & Pan, H. (2016). Solvent-free manufacturing of electrodes for lithium-ion batteries. *Scientific reports*, 6(1), 23150.
- [31] Miranda, A., Sarang, K., Gendensuren, B., Oh, E. S., Lutkenhaus, J., & Verduzco, R. (2020). Molecular design principles for polymeric binders in silicon anodes. *Molecular Systems Design & Engineering*, 5(4), 709-724.
- [32] Li, S., Liu, Y. M., Zhang, Y. C., Song, Y., Wang, G. K., Liu, Y. X., ... & Guo, X. D. (2021). A review of rational design and investigation of binders applied in silicon-based anodes for lithium-ion batteries. *Journal of Power Sources*, 485, 229331.
- [33] Lingappan, N., Kong, L., & Pecht, M. (2021). The significance of aqueous binders in lithium-ion batteries. *Renewable and Sustainable Energy Reviews*, 147, 111227.
- [34] Hong, X., Jin, J., Wen, Z., Zhang, S., Wang, Q., Shen, C., & Rui, K. (2016). On the dispersion of lithium-sulfur battery cathode materials effected by electrostatic and stereo-chemical factors of binders. *Journal of Power Sources*, 324, 455-461.
- [35] Dou, W., Zheng, M., Zhang, W., Liu, T., Wang, F., Wan, G., ... & Tao, X. (2023). Review on the binders for sustainable high-energy-density lithium ion batteries: status, solutions, and prospects. *Advanced Functional Materials*, 33(45), 2305161.
- [36] Loeffler, N., Kopel, T., Kim, G. T., & Passerini, S. (2015). Polyurethane binder for aqueous processing of Li-ion battery electrodes. *Journal of the Electrochemical Society*, 162(14), A2692.
- [37] Chou, S. L., Pan, Y., Wang, J. Z., Liu, H. K., & Dou, S. X. (2014). Small things make a big difference: binder effects on the performance of Li and Na batteries. *Physical Chemistry Chemical Physics*, 16(38), 20347-20359.
- [38] Zou, F., & Manthiram, A. (2020). A review of the design of advanced binders for high-performance batteries. *Advanced Energy Materials*, 10(45), 2002508.
- [39] Bresser, D., Buchholz, D., Moretti, A., Varzi, A., & Passerini, S. (2018). Alternative binders for sustainable electrochemical energy storage—the transition to aqueous electrode processing and bio-derived polymers. *Energy & Environmental Science*, 11(11), 3096-3127.

- [40] Cholewinski A, Si P, Uceda M, Pope M, Zhao B. Polymer Binders: Characterization and Development toward Aqueous Electrode Fabrication for Sustainability. *Polymers*. 2021; 13(4):631.
- [41] Wang, Y. B., Yang, Q., Guo, X., Yang, S., Chen, A., Liang, G. J., & Zhi, C. Y. (2022). Strategies of binder design for high-performance lithium-ion batteries: a mini review. *Rare Metals*, 1-17.
- [42] Liu, Y., Shao, R., Jiang, R., Song, X., Jin, Z., & Sun, L. (2023). A review of existing and emerging binders for silicon anodic Li-ion batteries. *Nano Research*, 1-17.
- [43] Shen, H., Wang, Q., Chen, Z., Rong, C., & Chao, D. (2023). Application and Development of Silicon Anode Binders for Lithium-Ion Batteries. *Materials*, 16(12), 4266.
- [44] Deng, L., Zheng, Y., Zheng, X., Or, T., Ma, Q., Qian, L., ... & Chen, Z. (2022). Design criteria for silicon-based anode binders in half and full cells. *Advanced Energy Materials*, 12(31), 2200850.
- [45] Li, Y., Wu, Y., Wang, Z., Xu, J., Ma, T., Chen, L., ... & Wu, F. (2022). Progress in solvent-free dry-film technology for batteries and supercapacitors. *Materials Today*, 55, 92-109.
- [46] Zhou, H., Liu, M., Gao, H., Hou, D., Yu, C., Liu, C., ... & Chen, D. (2020). Dense integration of solvent-free electrodes for Li-ion superbattery with boosted low temperature performance. *Journal of Power Sources*, 473, 228553.
- [47] Li, Y., Wu, Y., Wang, Z., Xu, J., Ma, T., Chen, L., ... & Wu, F. (2022). Progress in solvent-free dry-film technology for batteries and supercapacitors. *Materials Today*, 55, 92-109.
- [48] Hippauf, F., Schumm, B., Doerfler, S., Althues, H., Fujiki, S., Shiratsuchi, T., ... & Kaskel, S. (2019). Overcoming binder limitations of sheet-type solid-state cathodes using a solvent-free dry-film approach. *Energy Storage Materials*, 21, 390-398.
- [49] Kim, H. M., Yoo, B. I., Yi, J. W., Choi, M. J., & Yoo, J. K. (2022). Solvent-Free Fabrication of Thick Electrodes in Thermoplastic Binders for High Energy Density Lithium-Ion Batteries. *Nanomaterials*, 12(19), 3320.
- [50] Zhang, Y. (2023). Solvent-Free Electrode Fabrication Based on Polytetrafluoroethylene Fibrillation for Lithium-ion Batteries.
- [51] Zhang, Y., Huld, F., Lu, S., Jektvik, C., Lou, F., & Yu, Z. (2022). Revisiting polytetrafluoroethylene binder for solvent-free lithium-ion battery anode fabrication. *Batteries*, 8(6), 57.
- [52] Wang, X., Chen, S., Zhang, K., Huang, L., Shen, H., Chen, Z., ... & Jiang, Z. (2023). A Polytetrafluoroethylene-Based Solvent-Free Procedure for the Manufacturing of Lithium-Ion Batteries. *Materials*, 16(22), 7232.
- [53] Schällicke, G., Landwehr, I., Dinter, A., Pettinger, K. H., Haselrieder, W., & Kwade, A. (2020). Solvent-Free Manufacturing of Electrodes for Lithium-Ion Batteries via Electrostatic Coating. *Energy Technology*, 8(2), 1900309.

- [54] Al-Shroofy, M., Zhang, Q., Xu, J., Chen, T., Kaur, A. P., & Cheng, Y. T. (2017). Solvent-free dry powder coating process for low-cost manufacturing of $\text{LiNi}_{1/3}\text{Mn}_{1/3}\text{Co}_{1/3}\text{O}_2$ cathodes in lithium-ion batteries. *Journal of Power Sources*, 352, 187-193.
- [55] Lai, L. S., & Kokini, J. L. (1991). Physicochemical changes and rheological properties of starch during extrusion (a review). *Biotechnology progress*, 7(3), 251-266.
- [56] Bauer, W., & Nötzel, D. (2014). Rheological properties and stability of NMP based cathode slurries for lithium ion batteries. *Ceramics International*, 40(3), 4591-4598.
- [57] Gendensuren, B., He, C., & Oh, E. S. (2020). Preparation of pectin-based dual-crosslinked network as a binder for high performance Si/C anode for LIBs. *Korean Journal of Chemical Engineering*, 37, 366-373.
- [58] Weng, Z., Di, S., Chen, L., Wu, G., Zhang, Y., Jia, C., ... & Chen, G. (2022). Random Copolymer Hydrogel as Elastic Binder for the SiO_x Microparticle Anode in Lithium-Ion Batteries. *ACS Applied Materials & Interfaces*, 14(37), 42494-42503.
- [59] Zhong, X., Han, J., Chen, L., Liu, W., Jiao, F., Zhu, H., & Qin, W. (2021). Binding mechanisms of PVDF in lithium ion batteries. *Applied Surface Science*, 553, 149564.
- [60] Son, B., Ryou, M. H., Choi, J., Lee, T., Yu, H. K., Kim, J. H., & Lee, Y. M. (2014). Measurement and analysis of adhesion property of lithium-ion battery electrodes with SAICAS. *ACS applied materials & interfaces*, 6(1), 526-531.
- [61] Wang, H., Ge, W., Li, W., Wang, F., Liu, W., Qu, M. Z., & Peng, G. (2016). Facile fabrication of ethoxy-functional polysiloxane wrapped $\text{LiNi}_{0.6}\text{Co}_{0.2}\text{Mn}_{0.2}\text{O}_2$ cathode with improved cycling performance for rechargeable Li-ion battery. *ACS Applied Materials & Interfaces*, 8(28), 18439-18449.